Research Square

Preprints are preliminary reports that have not undergone peer review.
They should not be considered conclusive, used to inform clinical practice,
or referenced by the media as validated information.

Distributed cortical learning through LEC-mediated γ-synchrony

Ji-Song Guan

guanjs@shanghaitech.edu.cn

School of Life Sciences and Technology, ShanghaiTech University https://orcid.org/0000-0001-5219-0289

Di Yun

School of Life Science and Technology, ShanghaiTech University

Zheng Wang

School of Life Science and Technology, ShanghaiTech University

Shenglin Zhao

School of Life Science and Technology, ShanghaiTech University

Zhenjie Wang

School of Biomedical Engineering, ShanghaiTech University

Haoran Ma

Shanghai Institute of Optics and Fine Mechanics, Chinese Academy of Sciences

Fei He

Shanghai Institute of Optics and Fine Mechanics, Chinese Academy of Sciences

Junfeng Lu

Huashan Hospital, Fudan University https://orcid.org/0000-0002-6091-5742

Yuanning Li

School of Biomedical Engineering, ShanghaiTech University

Hong Xie

Institute of Photonic Chips, University of Shanghai for Science and Technology https://orcid.org/0000-0002-9165-8515

Article

Keywords:

Posted Date: October 27th, 2025

DOI: https://doi.org/10.21203/rs.3.rs-7826395/v1

License: This work is licensed under a Creative Commons Attribution 4.0 International License.
Read Full License

Additional Declarations: There is **NO** Competing Interest.

Version of Record: A version of this preprint was published at Nature Communications on September 1st, 2026. See the published version at https://doi.org/10.1038/s41467-026-77266-w.

Title: Distributed cortical learning through LEC-mediated γ-synchrony

Authors: Di Yun[1,4,9], Zheng Wang[1,4,9], Shenglin Zhao[1,4], Zhenjie Wang[2,4], Haoran Ma[6,8], Fei He[6,7], Junfeng Lu[5], Yuanning Li[2,4], Hong Xie[3]*, Ji-Song Guan[1,4]*

Affiliations:

[1]School of Life Science and Technology, ShanghaiTech University; Shanghai, 201210, China.

[2]School of Biomedical Engineering, ShanghaiTech University; Shanghai, 201210, China.

[3]Institute of Photonic Chips, School of Artificial Intelligence Science and Technology, University of Shanghai for Science and Technology; Shanghai, 200093, China.

[4]State Key Laboratory of Advanced Medical Materials and Devices, ShanghaiTech University; Shanghai, 201210, China.

[5]Department of Neurosurgery, Huashan Hospital, Shanghai Medical College, Fudan University; Shanghai, 200040, China.

[6]Shanghai Institute of Optics and Fine Mechanics, Chinese Academy of Sciences; Shanghai, 201800, China.

[7]Zhangjiang Laboratory; Shanghai, 201210, China.

[8]School of Physical Sciences, University of Science and Technology of China; Hefei, 230026, Anhui, China.

[9]These authors contributed equally to this work.

*Corresponding author.

Email: hongxie@usst.edu.cn (H.X.); guanjs@shanghaitech.edu.cn (J.-S.G.)

Abstract: Despite the well-established theoretical and experimental foundations of dopamine-driven reinforcement learning, how the reward prediction error (RPE) teaching signal modifies specific cortical memory networks remains unclear. Neural oscillations are crucial for the temporal binding of activities across distributed cell ensembles. Here, we identify that lateral entorhinal cortex layer 5 (LEC^5) mediated intercortical γ-synchrony is a neural correlate of the RPE signal derived from dopamine neurons in the ventral tegmental area (VTA^{DA}). The VTA^{DA}-LEC^5 circuit-based intercortical γ-synchrony facilitates both learning and memory retention, and at the single-cell level, entrains the activity of cortical latent Engrams. Human brain recordings also demonstrate a universal role of γ-synchrony in the processing of prediction errors. These findings suggest that LEC^5-mediated intercortical γ-synchrony serves as the nexus connecting reinforcement learning with the formation of cortical memory networks.

Main text:

Learning helps animals adapt to environmental changes much more rapidly than evolution does. Internalizing the acquired knowledge into lasting modifications within the neural networks facilitates prompt and energy-efficient responses to analogous situations rooted in previous experience. The temporal-difference learning (TD learning) model and the dopamine-driven RPE signal have emerged as fundamental principles of reinforcement learning for both artificial agents and biological organisms[1-4]. On the other hand, event-related Engrams, which are characterized as the cellular substrates responsible for the encoding and retrieval of long-term memory[5,6], are temporally localized within a specific time window and are sparsely distributed throughout the brain[7-9]. This raises a fundamental question: how does the RPE teaching signal coordinate this sparse yet extensive Engram network in the brain?

Widespread neural oscillations across a spectrum of frequencies provide various temporal windows for instantaneous communications among segregated brain areas, reflecting diverse modes of functional connectivity in neural networks during information processing[10-13]. Gamma band oscillations (γ-oscillations) were implicated in associative learning and memory storage processes in both mice and humans[14-16]. Furthermore, our prior research demonstrated that artificially inducing the synchronization of cortical γ-oscillations (intercortical γ-synchrony) via stimulation of the LEC[5] reinstated contextual memory formation and retrieval in mice with hippocampal lesions[17]. Nonetheless, the precise biological function of intercortical γ-synchrony in learning and memory remains unclear.

In this study, we explored the correlation between the intercortical γ-synchrony and the dopamine-driven RPE signal. We combined fiber photometry, electrophysiology recordings, and two-photon (2P) imaging techniques to uncover the underlying neural circuit mechanisms. Moreover, we verified the causal relationship between circuit-based intercortical γ-synchrony and animal behaviors. At the single-cell level, to understand how intercortical γ-synchrony entrains the activity of latent cortical Engrams, we recorded calcium activity in retrosplenial cortex (RSC) neurons and local field potentials (LFPs) in both RSC and auditory cortex (AuD) simultaneously through a combination of 2P microscopy and ultraflexible electrode arrays. Finally, we conducted electrocorticography (ECoG) recordings in human brains during a real-phrases or pseudo-phrases reading task to examine the cross-species generalizability of intercortical γ-synchrony in the processing of prediction error.

Intercortical γ-synchrony reflects the RPE signal processing

In Pavlovian conditioning, through trial and error, anticipation of the unconditioned stimulus (US) following the neutral conditioned stimulus (CS) is indicative of adaptive changes made by the nervous system. We designed a Pavlovian tone-reward (CS-US) association learning paradigm with specific trial structures. LFPs from three task-related cortical regions, including RSC, AuD, and the secondary motor cortex (M2), were recorded during the behavior experiment (Fig. 1a). The strength of theta-coupled synchrony (by subsampling LFPs to theta trough) between pairwise oscillations can be quantified using the phase-locking value (PLV)[17]. Elevated PLV indicates a stable pairwise phase difference, suggesting increased coordinated activity between two brain regions.

Initially, we exposed water-restricted mice (n = 13) to ten CS-only trials and ten US-only trials, respectively. No significant pairwise PLV change was observed during the CS-only trials. Conversely, after receiving a reward in the US-only trials, there were significant increases (13.50 ± 1.71%) in intercortical γ-synchrony (20–40 Hz, averaged across three pairs: RSC-AuD, RSC-M2, and AuD-M2) compared to the baseline (Fig. 1b). Additionally, the levels of theta band (6–10 Hz) synchrony (Fig. 1c) and theta-gamma modulation index (Fig. 1d) also increased, indicating stronger cross-frequency coupling. The conjecture that licking behavior contributed to the increase in intercortical γ-synchrony is not supported by a comparison of the PLV between periods when mice engaged in licking water and periods when they did not (Extended Data Fig. 1a). There was no significant difference in the extent to which each pair contributed to the increase in γ-synchrony (Extended Data Fig. 1b). The power of γ-oscillations was unchanged in the three cortex regions (Extended Data Fig. 1c). Our prior work also showed that intercortical γ-synchrony is unaffected by volume conduction[17].

All mice underwent daily 100 CS-US associative trials throughout training from day 1 to day 6. In each trial, the CS tone persists for 1 second, followed by a 1-second delay, then a 2-second response window. Only licking the water pipe within the response window will trigger the infrared sensor to pump a drop of water as a reward. Each trial is separated by a 5–8 seconds inter-trial interval (ITI), followed by a 4–6 seconds lick-withhold period (Fig. 1e). After six days of training, the average behavioral performance reached 84.31 ± 4.60%, attaining a proficient level, with licking movements progressively stabilizing within the response window (Fig. 1f and Extended Data Fig. 1d). A day-by-day analysis of the PLV changes revealed a backward shift in intercortical γ-synchrony from the response window (2 to 4 s) to the CS lasting period (0 to 1 s) as associative training progressed (Fig. 1g). Moreover, intercortical γ-synchrony within the response window gradually declined, while it exhibited an opposite trend during the CS period (Fig. 1h).

Based on the TD learning model, it can be inferred that the RPE signal traces back to the earliest cue capable of predicting rewards and terminates there, as no earlier predictive signal exists than this one[4]. To further confirm the relationship between the γ-synchrony backward shift phenomenon and RPE signal encoding, we conducted a CS replacing experiment on day 7 with six proficient mice from the earlier CS-US association training. In this experiment, a blue light cue (CS2, -1 to 0 s) was presented ahead of the identical tone cue (CS1) (Fig. 1i). The average behavioral performance exceeded 70% on day 7 (Extended Data Fig. 1e). Once again, the enhancement of γ-synchrony diminished during the CS1 period (devalued) and persisted in shifting backward in time towards CS2 (Fig. 1j–l).

Finally, to assess the sensitivity of intercortical γ-synchrony in reflecting the dynamic trial-by-trial fluctuations in the RPE signal, we adjusted the CS-US contingency by randomly varying the US size in each trial on day 7 for the other seven remaining proficient mice (Fig. 1m). The average behavioral performance surpassed 70% on day 7 (Extended Data Fig. 1f). According to the TD learning algorithm, rewards that surpass expectations elicit a positive RPE signal, whereas rewards that fall below expectations generate a negative RPE signal. The trial-by-trial relative changes in RPE values following the delivery of different rewards to mice can be calculated iteratively[18]. During the iterative calculations, trials in which animals abstained from water-licking activities throughout the entire duration from CS to ITI were excluded, as such trials signified

incomplete engagement with the environment. The relative difference in the average intercortical γ-synchrony between the baseline and response window for trials excluded due to lack of action was not statistically significant (Extended Data Fig. 1g). The initial expectation of reward (*VI*) for each mouse was set to its hit rate on day 6, with a learning rate (α) of 0.5. Linear fitting analysis demonstrated a statistically significant positive correlation between the relative PLV change within the response window (compared to baseline, -6 to 0 s) and the current RPE update, in contrast to the PLV change within the pre-trial period (-2 to 0 s) (Fig. 1n, o).

Intercortical γ-synchrony correlates with the VTA^{DA} activity

We then used fiber photometry and LFP recordings to measure the correlation between the intercortical γ-synchrony and VTA^{DA} population activities during associative learning in DAT-Cre mice (Fig. 2a, b). The training paradigm was consistent with that depicted in Fig. 1e. As training progressed, the enhancement of intercortical γ-synchrony during the CS period and the calcium activities of VTA^{DA} were positively correlated (Fig. 2c, d and Extended Data Fig. 2a). Notably, the time lag between the onset of calcium activities in the VTA^{DA} population during the CS period and the increase in intercortical γ-synchrony on day 6 revealed that VTA^{DA} activity preceded the rise in PLV (-0.18 ± 0.04 s), indicating that VTA^{DA} is upstream in the RPE information cascade. (Fig. 2e). Furthermore, optogenetic stimulation of the unilateral VTA^{DA} at 20 Hz (approximating the VTA^{DA} phasic firing rate[4]) elicited a consistent augmentation (82.47 ± 9.12%) in ipsilateral intercortical γ-synchrony following a brief delay (0.45 ± 0.05 s, Fig. 2f–i). Following VTA^{DA} stimulation, a discernible upward trend in γ-synchrony was observed between the LEC and cortices, as well as in LEC γ-oscillation power (Extended Data Fig. 2b–f). Additionally, the γ-oscillation power in the RSC, AuD, and M2 significantly enhanced (Extended Data Fig. 2e, f).

LEC^5 relays the RPE signal to the cortex

We conducted optetrode recordings in the pan layer 5 driver line Rbp4-Cre mice (Fig. 2j–l and Extended Data Fig. 3a). Following the receipt of the reward in the US-only trials, the mean firing rates of eleven photo-identified Rbp4-positive units (well-isolated from six mice) increased significantly by 5.66 ± 0.59 Hz from the baseline. In comparison to the baseline of CS-only trials, there was no statistically significant increase in the firing rate during the CS period. However, as the training progressed, there was a notable increase in firing rate by 2.30 ± 0.55 Hz during the CS period, which was consistent with the firing pattern associated with RPE encoding in VTA^{DA}. We did not observe a distinct distribution of spike probability in Rbp4-positive cells over theta phases or low gamma phases through circular vector analysis (Extended Data Fig. 3b).

Given our previous research indicating a strong link between intercortical γ-synchrony and LEC^5, it is essential to investigate the mediating role of LEC^5 in transferring the RPE signal from VTA^{DA} to the cortex[17]. In alignment with prior research, our anterograde trans-synaptic tracing experiments showed that cortical neurons downstream of LEC^5 are predominantly located in the superficial layers, with only a limited subset of these downstream cells expressing parvalbumin (Extended Data Fig. 4).

To investigate afferent activity from LEC^5 to the cortex, we recorded axonal calcium activities of LEC^5-RSC projections using a 2P microscope (1466 boutons from seven mice, Fig. 2m, n), followed by noise reduction (Extended Data Fig. 5a, b). In the CS-only and US-only trials, 10.9% of the boutons were classified as CS-responsive, 20.8% as US-responsive, and 6.0% as CS/US co-responsive (Fig. 2o, p). Interestingly, a significant reduction in the mean activity of a considerable portion of the US-responsive boutons was observed during the final five US-only trials in comparison to the initial five trials, indicating habituation to the unexpected US presentation (Fig. 2q). Due to the limited photostability of untargeted GCaMP6s in axons, maintaining a stable field of view across multiple days is challenging. As a compromise, a swift experiment comprising 30 trials with varying US sizes was conducted (Fig. 2r), and the response window was substituted with direct reward delivery (exemption from triggering) to expedite the imaging process. In the initial series of fifteen CS-US association trials, 25.5% of the boutons exhibited responses. In the following three series of trials—comprising five double US trials with two drops of water, five US omission trials without water delivery, and an additional set of five CS-US association trials with one drop of water—6.6% of boutons conformed to the TD learning model. The activity of these TD-boutons during the US period exhibited three distinct patterns in relation to the activity levels observed during the initial series of CS-US trials (0.086 ± 0.008, dF/F0): an elevation in activity when the reward was doubled (0.179 ± 0.013, dF/F0), a reduction when the reward was omitted (-0.014 ± 0.004, dF/F0), and a renewed increase upon the reintroduction of the reward (0.091 ± 0.012, dF/F0). Notably, this result cannot be attributed solely to the reflection of reward sizes rather than learning, as averaged responses exceeding 0.05 (dF/F0) were observed in all four series of trials during the CS period, but not in the preceding CS-only trials (Fig. 2s–v). We classified these 97 TD-boutons into 70 independent axons based on distinct distribution patterns between intra-axonal and inter-axonal correlation coefficients (Extended Data Fig. 5c, d).

These data collectively suggest a bottom-up hierarchical cascade, whereby the RPE signal is initially conveyed from the VTA^{DA} to LEC^5, and culminating in an enhancement of intercortical γ-synchrony through common afferent excitatory projections from LEC^5 (Fig. 2w).

VTA^{DA}-LEC^5 pathway facilitates associative learning

Numerous studies have established the causal role of VTA^{DA} as a TD learning signal in the brain. Activating or inhibiting VTA^{DA} can effectively influence the associative learning process in mice[19-24] and non-human primates[25]. To examine the necessity of the VTA^{DA}-LEC^5 circuit in associative learning behaviors, we first conducted a loss-of-function experiment by time-locked optogenetic inhibition of VTA^{DA}-LEC dopamine projections. In each trial, a 589 nm laser was applied continuously for 3 seconds, covering the delay period and the response window during the entire associative training (Fig. 3a–c). Notably, dopaminergic afferent projections in the LEC region are distributed not only in the superficial layers but also extend into the deep layers (Fig. 3b). Compared to the mCherry control group, inhibiting VTA^{DA} projections to LEC impaired the learning performance of mice (Fig. 3f). A comparison of the relative PLV change during the CS period on day 6 between the inhibition group and the control group showed that the levels of intercortical γ-synchrony significantly increased by 34.78 ± 4.93% in the control group, while it

remained unchanged (-1.13 ± 2.04%) in the inhibition group (Fig. 3d, e and Extended Data Fig. 6a).

Subsequently, we activated LEC^5 while simultaneously suppressing upstream VTA^{DA}-LEC projections in DAT-Cre × Rbp4-Cre mice during the entire associative training (Fig. 3g–i). Mice in the experimental group showed significantly better performance compared to the group that received solely VTA^{DA}-LEC inhibition (Fig. 3l, left). Strikingly, the performance disparities between the groups were discernible even in the initial stages of the training process, indicating accelerated learning (Fig. 3l, right). Furthermore, the relative change in PLV during the CS period on day 6 between the groups showed that intercortical γ-synchrony increased significantly (22.21 ± 3.72%) in the experimental group mice, while it remained unchanged (-1.73 ± 1.46%) in the inhibition-only group (Fig. 3j, k and Extended Data Fig. 6b). Notably, the increase in PLV observed during the delay and response intervals was attributable to laser stimulation, whereas the enhancement within the CS period was endogenous (Fig. 3j).

Stimulation of LEC^5 improves contextual memory retention

To examine whether LEC^5-mediated intercortical γ-synchrony improves learning and memory retention in more complex tasks beyond CS-US associative trials, we conducted two experiments involving contextual associations: reward-tropism conditioned place preference (CPP) and punishment-tropism contextual fear conditioning (CFC), both of which require continuous sensory feedback during environmental navigation (Fig. 3m, p).

The initial day of the CPP experiment demonstrated that mice subject to dietary restrictions exhibited a preference for the dark side of the light-dark box. On the second day, we separated the two boxes and allowed the mice to explore for ten minutes. Mice were exposed to 30 Hz laser stimulation throughout foraging in the isolated light box with buried food. In the subsequent test conducted on day 3, the light and dark compartments were interconnected, and both the oChIEF group and the mCherry group of mice spent more time exploring the bright side of the box, where food had previously been buried. However, in the test conducted on day 5, only the oChIEF group mice continued to spend more time exploring the bright side, indicating stable long-term memory retention. In contrast, the mCherry group of mice reinstated their preference for dark environments (Fig. 3n, o).

In the CFC experiment, mice were subjected to a mild electrical foot shock (0.3 mA, 2 seconds), followed by three minutes of optogenetic stimulation of LEC^5. There were no significant differences between the mCherry control group (n = 9) and the oChIEF group (n = 8) in travel distance during the 3-minute habituation period or in running speed during the foot shock (Extended Data Fig. 6c, d). No observable difference in freezing levels was noted between the oChIEF group (40.56 ± 8.42%) and the mCherry group (45.02 ± 6.13%) during the immediate recall of fear memory. However, 24 hours later, only the oChIEF group preserved elevated freezing levels (46.98 ± 8.59%) during the second recall test, indicating a robust fear memory retention. (Fig. 3q). Given its bidirectional enhancement of both positive and negative memory, the VTA^{DA}-LEC^5 circuit may contribute to the computation of contextual prediction errors within the neocortex.

Intercortical γ-synchrony entrains the activities of the latent RSC Engrams

To determine whether intercortical γ-synchrony is a cause or a consequence of cortical neural activities, it is essential to understand its function from a cellular perspective. We recorded the calcium activities of RSC neurons using a two-photon (2P) microscope, while concurrently employing custom-made 2-shank ultraflexible electrode arrays [26] or tungsten electrodes, to record LFPs from both the RSC and AuD regions (Fig. 4a–c and Extended Data Fig. 7a, c). Calcium activities of a total of 685 neurons from eight mice were recorded during the CS-only and US-only stimulation epochs on day 1, during the CS-US association learning epoch on day 3, and during the memory recall epoch on day 7 (Fig. 4d and Extended Data Fig. 7d, e). The trial-averaged responses observed in the initial experiments indicated that a certain percentage of cells responded to the CS stimulus (4.67%), the US stimulus (34.01%), and both the CS and US stimuli (9.49%). Excluding two CS-only encoding neurons and 17 US-only encoding neurons throughout the entire experiment, 93 neurons exhibited responses to either the CS, the US, or both during the association training on day 3. These neurons were categorized within the association-encoding group (Asso.). On day 7, all mice demonstrated proficient performance, with 78 neurons exhibiting activity confined to narrow windows within the CS period. We classified these neurons as recall group cells (Recall). Next, we retraced the activity of these Recall cells on day 3 and found that 18 cells (2.63% of the total) had previously been categorized within the Asso. group, exhibiting transient activity during both the learning and recall stages (Fig. 4e). We classify these 18 cells as latent cortical Engrams that maintain associative memory.

In mice implanted with ultraflexible electrode arrays, it was observed that the selection of either deep or superficial oscillations influenced the calculation of γ-synchrony (Extended Data Fig. 7b). Consistent with experiments employing tungsten electrodes inserted into the superficial cortical layer, superficial LFPs were selected for the computation of RSC-AuD γ-synchrony. In comparing the correlations between RSC single-cell calcium activities and the concurrent RSC-AuD pairwise PLV change on day 3, the correlation coefficient for the RSC latent Engram group was significantly higher than that for the non-Engram group (Fig. 4, f–h). Crucially, the increase in PLV preceded the rising time point of calcium activities (-0.21 ± 0.13 s) in the RSC latent Engrams on day 3, indicating that γ-synchrony entrains the activities of the latent RSC Engrams during learning. Given the unique projections of LEC[5] to various cortical regions, we hypothesize that mechanisms similar to those observed in the RSC may also exist in other areas. Nonetheless, a notable decrease in the time lag (0.15 ± 0.05 s) between calcium activity of these latent RSC Engrams and the increase in PLV was observed on day 7 (Fig. 4i).

Based on these results, we suggest that the LEC-mediated γ-synchrony signal precedes the activation of the latent Engram during the initial phases of learning. Conversely, once the mice reach the proficient level, the activation of the Engram network occurs before the emergence of the intercortical γ-synchrony signal, indicating an intercortical γ-synchrony-mediated mechanism for the maturation of the cortical memory networks (Fig. 4j).

Enhancement of γ-synchrony in the human brain during prediction error processing

The dopamine-driven RPE teaching signal has been observed in several species, including Drosophila [27], zebra finches [28], and humans [29], demonstrating its conserved feature across species.

Furthermore, neural representations of broadly defined prediction errors (discrepancies between expectations and perceptions) have recently extended beyond cue-reward associations to include areas such as social interaction[30,31], threat avoidance[32], addiction[33], pain expectation[34], and speech perception [35], highlighting the functional diversity of prediction error signals in the brain.

We performed a reading task with patients undergoing awake glioma resection with language mapping (Fig. 5a, b). High-density ECoG grids were placed intraoperatively over the temporal, frontal, and parietal lobes to record LFPs (Extended Data Fig. 8a and Extended Table 3, 4). Each trial consisted of three sequential phases: an initial fixation period of 1 second, during which a central crosshair was displayed; a perception phase of 2 seconds, during which two-character Mandarin phrase stimuli were presented on the screen; and a subsequent reading phase of 1.5 seconds. Sound waves during articulation were recorded to verify an accurate reading. The stimuli comprised three real-phrases and three pseudo-phrases. Each phrase was reiterated three times in random sequence within a single block, with several minutes of rest between the two blocks, culminating in a total of six repetitions per phrase. Data from the initial block showed that parietal-parietal synchrony (20–25 Hz) increased when perceiving pseudo-phrases (11.88 ± 3.90%) compared to real-phrases (0.44 ± 2.62%), indicating cortical processing of prediction errors. Furthermore, the enhancement in synchrony diminished in the subsequent block (0.23 ± 2.57%), suggesting rapid familiarization with pseudo-phrases based on knowledge acquired in the first block (Fig. 5c, d and Extended Data Fig. 8b). Additionally, no significant alterations in the power of γ-oscillations within the parietal lobe region were observed (Extended Data Fig. 8c).

Discussion

In this study, we observed a remarkable resemblance between the patterns of intercortical γ-synchrony and the dopamine-driven RPE signal in both mice and humans, indicating that the neural signature of the RPE signal within cortical areas is represented as intercortical γ-synchrony. Growing evidence shows that RPE-encoding cell populations exist in the neocortex[36-38]. However, it remains unclear how these higher regions update current predictions when they no longer match the real-world conditions. Our study reveals a previously unknown circuit architecture that transmits the midbrain dopamine RPE signal to the extensive cortical regions.

LEC has been documented to participate in temporal segmentation of episodic events[39], and reward learning[40,41]. Two studies from the Igarashi laboratory clarify the pivotal function of VTA projections to the fan cells within the LEC layer L2a, as well as the bidirectional loop circuit between the medial prefrontal cortex and the deep-layer LEC, in learning odor-based associations[42,43]. Notably, the entorhinal region has also been identified as a primary area of vulnerability in the early stages of Alzheimer's disease[44]. In line with these advances in LEC research, our study deepens the understanding of LEC's role in the processing of the RPE signal. The RPE-driven retrospective reinforcement mechanism enables animals to infer the specific actions that elicit dopamine release[45]. Such associations constitute the fundamental framework of memory formation. We confirmed that the bottom-up VTA^{DA}-LEC^5 RPE signal cascade is not only essential but also sufficient for supporting associative learning and memory retention. Fine-tuning LEC^5 activity may facilitate the differentiated development of specialized neural networks tailored to specific memories.

Given the ambiguity regarding the origin and significance of LFPs, despite extensive research into the relationship between neural oscillations and cognitive functions, the spectral pattern of a particular oscillation is often questioned as an epiphenomenon that merely reflects the dynamic mode of neural networks rather than acting as a causal factor in specific neural activities[46]. At the single-cell level, we discovered that instantaneous intercortical γ-synchrony functions as a reference point for entraining the activities of RSC latent Engrams during reinforcement learning at the early stage. Neuronal spike probability in a particular phase of oscillation can be modulated by the extracellular electric field, which may orchestrate the spike timing of distributed cell ensembles and guide the formation of intercortical connections[47,48]. Considering that γ-oscillations are more localized in time and space[46], our data indicate that common inputs from the LEC[5] facilitate the integration of functionally segregated cortical regions through intercortical synchrony at the low gamma band. Notably, we observed that cortical Engram activity precedes the increase in intercortical γ-synchrony during memory recall (Fig. 4i, j), indicating a mechanism mediated by intercortical γ-synchrony for the development of cortical memory networks.

Entrainment to a specific frequency of oscillation is cell-type dependent. Inhibitory neurons play a crucial role in regulating γ-oscillations[49,50]. Further investigation is required to elucidate the mechanisms underlying the local processing of afferent information from LEC[5] within the cortical microcircuit and to understand its implications in intercortical connections.

References

1 Sutton, R. S. & Barto, A. G. Toward a modern theory of adaptive networks: expectation and prediction. *Psychol Rev* **88**, 135-170 (1981). https://doi.org/10.1037/0033-295X.88.2.135

2 Schultz, W., Dayan, P. & Montague, P. R. A neural substrate of prediction and reward. *Science* **275**, 1593-1599 (1997). https://doi.org:10.1126/science.275.5306.1593

3 Montague, P. R., Dayan, P. & Sejnowski, T. J. A framework for mesencephalic dopamine systems based on predictive Hebbian learning. *J Neurosci* **16**, 1936-1947 (1996). https://doi.org:10.1523/JNEUROSCI.16-05-01936.1996

4 Glimcher, P. W. Understanding dopamine and reinforcement learning: the dopamine reward prediction error hypothesis. *Proc Natl Acad Sci U S A* **108 Suppl 3**, 15647-15654 (2011). https://doi.org:10.1073/pnas.1014269108

5 Liu, X. *et al.* Optogenetic stimulation of a hippocampal engram activates fear memory recall. *Nature* **484**, 381-385 (2012). https://doi.org:10.1038/nature11028

6 Josselyn, S. A. & Tonegawa, S. Memory engrams: Recalling the past and imagining the future. *Science* **367** (2020). https://doi.org:10.1126/science.aaw4325

7 Goode, T. D., Tanaka, K. Z., Sahay, A. & McHugh, T. J. An Integrated Index: Engrams, Place Cells, and Hippocampal Memory. *Neuron* **107**, 805-820 (2020). https://doi.org:10.1016/j.neuron.2020.07.011

8 Roy, D. S. *et al.* Brain-wide mapping reveals that engrams for a single memory are distributed across multiple brain regions. *Nat Commun* **13**, 1799 (2022). https://doi.org:10.1038/s41467-022-29384-4

9 Xie, H. *et al.* In vivo imaging of immediate early gene expression reveals layer-specific memory traces in the mammalian brain. *Proc Natl Acad Sci U S A* **111**, 2788-2793 (2014). https://doi.org:10.1073/pnas.1316808111

10 Buzsáki, G. & Vöröslakos, M. Brain rhythms have come of age. *Neuron* **111**, 922-926 (2023). https://doi.org:10.1016/j.neuron.2023.03.018

11 Fries, P. A mechanism for cognitive dynamics: neuronal communication through neuronal coherence. *Trends Cogn Sci* **9**, 474-480 (2005). https://doi.org:10.1016/j.tics.2005.08.011

12 Fries, P. Rhythms for Cognition: Communication through Coherence. *Neuron* **88**, 220-235 (2015). https://doi.org:10.1016/j.neuron.2015.09.034

13 Palmigiano, A., Geisel, T., Wolf, F. & Battaglia, D. Flexible information routing by transient synchrony. *Nat Neurosci* **20**, 1014-1022 (2017). https://doi.org:10.1038/nn.4569

14 Sohal, V. S. How Close Are We to Understanding What (if Anything) γ Oscillations Do in Cortical Circuits? *Journal of Neuroscience* **36**, 10489-10495 (2016). https://doi.org:10.1523/Jneurosci.0990-16.2016

15 Bastos, A. M. *et al.* Canonical microcircuits for predictive coding. *Neuron* **76**, 695-711 (2012). https://doi.org:10.1016/j.neuron.2012.10.038

16 Grover, S., Wen, W., Viswanathan, V., Gill, C. T. & Reinhart, R. M. G. Long-lasting, dissociable improvements in working memory and long-term memory in older adults

with repetitive neuromodulation. *Nat Neurosci* **25**, 1237-1246 (2022). https://doi.org:10.1038/s41593-022-01132-3

17 Luo, W. *et al.* Acquiring new memories in neocortex of hippocampal-lesioned mice. *Nat Commun* **13**, 1601 (2022). https://doi.org:10.1038/s41467-022-29208-5

18 Hamid, A. A. *et al.* Mesolimbic dopamine signals the value of work. *Nat Neurosci* **19**, 117-126 (2016). https://doi.org:10.1038/nn.4173

19 Chang, C. Y. *et al.* Brief optogenetic inhibition of dopamine neurons mimics endogenous negative reward prediction errors. *Nat Neurosci* **19**, 111-116 (2016). https://doi.org:10.1038/nn.4191

20 Sharpe, M. J. *et al.* Dopamine transients are sufficient and necessary for acquisition of model-based associations. *Nat Neurosci* **20**, 735-742 (2017). https://doi.org:10.1038/nn.4538

21 Saunders, B. T., Richard, J. M., Margolis, E. B. & Janak, P. H. Dopamine neurons create Pavlovian conditioned stimuli with circuit-defined motivational properties. *Nat Neurosci* **21**, 1072-1083 (2018). https://doi.org:10.1038/s41593-018-0191-4

22 Lee, K. *et al.* Temporally restricted dopaminergic control of reward-conditioned movements. *Nat Neurosci* **23**, 209-216 (2020). https://doi.org:10.1038/s41593-019-0567-0

23 Morrens, J., Aydin, C., Janse van Rensburg, A., Esquivelzeta Rabell, J. & Haesler, S. Cue-Evoked Dopamine Promotes Conditioned Responding during Learning. *Neuron* **106**, 142-153 (2020). https://doi.org:10.1016/j.neuron.2020.01.012

24 Lak, A. *et al.* Dopaminergic and Prefrontal Basis of Learning from Sensory Confidence and Reward Value. *Neuron* **105**, 700-711.e706 (2020). https://doi.org:10.1016/j.neuron.2019.11.018

25 Stauffer, W. R. *et al.* Dopamine Neuron-Specific Optogenetic Stimulation in Rhesus Macaques. *Cell* **166**, 1564-1571 (2016). https://doi.org:10.1016/j.cell.2016.08.024

26 Luan, L. *et al.* Ultraflexible nanoelectronic probes form reliable, glial scar-free neural integration. *Sci Adv* **3**, e1601966 (2017). https://doi.org:10.1126/sciadv.1601966

27 Bennett, J. E. M., Philippides, A. & Nowotny, T. Learning with reinforcement prediction errors in a model of the Drosophila mushroom body. *Nat Commun* **12**, 2569 (2021). https://doi.org:10.1038/s41467-021-22592-4

28 Gadagkar, V. *et al.* Dopamine neurons encode performance error in singing birds. *Science* **354**, 1278-1282 (2016). https://doi.org:10.1126/science.aah6837

29 Jang, A. I., Nassar, M. R., Dillon, D. G. & Frank, M. J. Positive reward prediction errors during decision-making strengthen memory encoding. *Nat Hum Behav* **3**, 719-732 (2019). https://doi.org:10.1038/s41562-019-0597-3

30 Solié, C., Girard, B., Righetti, B., Tapparel, M. & Bellone, C. VTA dopamine neuron activity encodes social interaction and promotes reinforcement learning through social prediction error. *Nat Neurosci* **25**, 86-97 (2022). https://doi.org:10.1038/s41593-021-00972-9

31 Xie, Y., Huang, L., Corona, A., Pagliaro, A. H. & Shea, S. D. A dopaminergic reward prediction error signal shapes maternal behavior in mice. *Neuron* **111**, 557-570.e557 (2023). https://doi.org:10.1016/j.neuron.2022.11.019

32 Akiti, K. *et al.* Striatal dopamine explains novelty-induced behavioral dynamics and individual variability in threat prediction. *Neuron* **110**, 3789-3804 e3789 (2022). https://doi.org:10.1016/j.neuron.2022.08.022

33 Konova, A. B. *et al.* Reduced neural encoding of utility prediction errors in cocaine addiction. *Neuron* **111**, 4058-4070.e4056 (2023). https://doi.org:10.1016/j.neuron.2023.09.015

34 Bott, F. S. *et al.* Local brain oscillations and interregional connectivity differentially serve sensory and expectation effects on pain. *Sci Adv* **9**, eadd7572 (2023). https://doi.org:10.1126/sciadv.add7572

35 Sohoglu, E., Beckers, L. & Davis, M. H. Convergent neural signatures of speech prediction error are a biological marker for spoken word recognition. *Nat Commun* **15**, 9984 (2024). https://doi.org:10.1038/s41467-024-53782-5

36 O'Toole, S. M., Oyibo, H. K. & Keller, G. B. Molecularly targetable cell types in mouse visual cortex have distinguishable prediction error responses. *Neuron* **111**, 2918-2928 (2023). https://doi.org:10.1016/j.neuron.2023.08.015

37 Furutachi, S., Franklin, A. D., Aldea, A. M., Mrsic-Flogel, T. D. & Hofer, S. B. Cooperative thalamocortical circuit mechanism for sensory prediction errors. *Nature* **633**, 398-406 (2024). https://doi.org:10.1038/s41586-024-07851-w

38 Drieu, C. *et al.* Rapid emergence of latent knowledge in the sensory cortex drives learning. *Nature* **641**, 960-970 (2025). https://doi.org:10.1038/s41586-025-08730-8

39 Kanter, B. R., Lykken, C. M., Polti, I., Moser, M. B. & Moser, E. I. Event structure sculpts neural population dynamics in the lateral entorhinal cortex. *Science* **388**, eadr0927 (2025). https://doi.org:10.1126/science.adr0927

40 Igarashi, K. M., Lu, L., Colgin, L. L., Moser, M. B. & Moser, E. I. Coordination of entorhinal-hippocampal ensemble activity during associative learning. *Nature* **510**, 143-147 (2014). https://doi.org:10.1038/nature13162

41 Issa, J. B., Radvansky, B. A., Xuan, F. & Dombeck, D. A. Lateral entorhinal cortex subpopulations represent experiential epochs surrounding reward. *Nat Neurosci* **27**, 536-546 (2024). https://doi.org:10.1038/s41593-023-01557-4

42 Lee, J. Y. *et al.* Dopamine facilitates associative memory encoding in the entorhinal cortex. *Nature* **598**, 321-326 (2021). https://doi.org:10.1038/s41586-021-03948-8

43 Jun, H. *et al.* Prefrontal and lateral entorhinal neurons co-dependently learn item-outcome rules. *Nature* **633**, 864-871 (2024). https://doi.org:10.1038/s41586-024-07868-1

44 Igarashi, K. M. Entorhinal cortex dysfunction in Alzheimer's disease. *Trends in Neurosciences* **46**, 124-136 (2023). https://doi.org:10.1016/j.tins.2022.11.006

45 Tang, J. C. Y. *et al.* Dynamic behaviour restructuring mediates dopamine-dependent credit assignment. *Nature* **626**, 583-592 (2024). https://doi.org:10.1038/s41586-023-06941-5

46 Fernandez-Ruiz, A., Sirota, A., Lopes-dos-Santos, V. & Dupret, D. Over and above frequency: Gamma oscillations as units of neural circuit operations. *Neuron* **111**, 936-953 (2023). https://doi.org:10.1016/j.neuron.2023.02.026

47 Luo, W. & Guan, J.-S. Do brain oscillations orchestrate memory? *Brain Science Advances* **4**, 16-33 (2018). https://doi.org:10.26599/BSA.2018.9050008

48 Lee, S. Y. *et al.* Cell-class-specific electric field entrainment of neural activity. *Neuron* **112**, 2614-2630.e2615 (2024). https://doi.org:10.1016/j.neuron.2024.05.009

49 Sohal, V. S., Zhang, F., Yizhar, O. & Deisseroth, K. Parvalbumin neurons and gamma rhythms enhance cortical circuit performance. *Nature* **459**, 698-702 (2009). https://doi.org:10.1038/nature07991

50 Veit, J., Handy, G., Mossing, D. P., Doiron, B. & Adesnik, H. Cortical VIP neurons locally control the gain but globally control the coherence of gamma band rhythms. *Neuron* **111**, 405-417 (2023). https://doi.org:10.1016/j.neuron.2022.10.036

51 Yin, R. *et al.* Chronic co-implantation of ultraflexible neural electrodes and a cranial window. *Neurophotonics* **9**, 032204 (2022). https://doi.org:10.1117/1.NPh.9.3.032204

52 Tort, A. B., Komorowski, R., Eichenbaum, H. & Kopell, N. Measuring phase-amplitude coupling between neuronal oscillations of different frequencies. *J Neurophysiol* **104**, 1195-1210 (2010). https://doi.org:10.1152/jn.00106.2010

53 Lachaux, J. P., Rodriguez, E., Martinerie, J. & Varela, F. J. Measuring phase synchrony in brain signals. *Hum Brain Mapp* **8**, 194-208 (1999). https://doi.org:10.1002/(sici)1097-0193(1999)8:4<194::aid-hbm4>3.0.co;2-c

54 Berens, P. CircStat: A MATLAB Toolbox for Circular Statistics. *Journal of Statistical Software* **31**, 1 - 21 (2009). https://doi.org:10.18637/jss.v031.i10

55 Liu, C. *et al.* Hippocampus alters visual representation to encode new memory. *Cell Rep* **44**, 115594 (2025). https://doi.org:10.1016/j.celrep.2025.115594

56 Li, X. *et al.* Real-time denoising enables high-sensitivity fluorescence time-lapse imaging beyond the shot-noise limit. *Nat Biotechnol* **41**, 282-292 (2023). https://doi.org:10.1038/s41587-022-01450-8

Main Figure 1

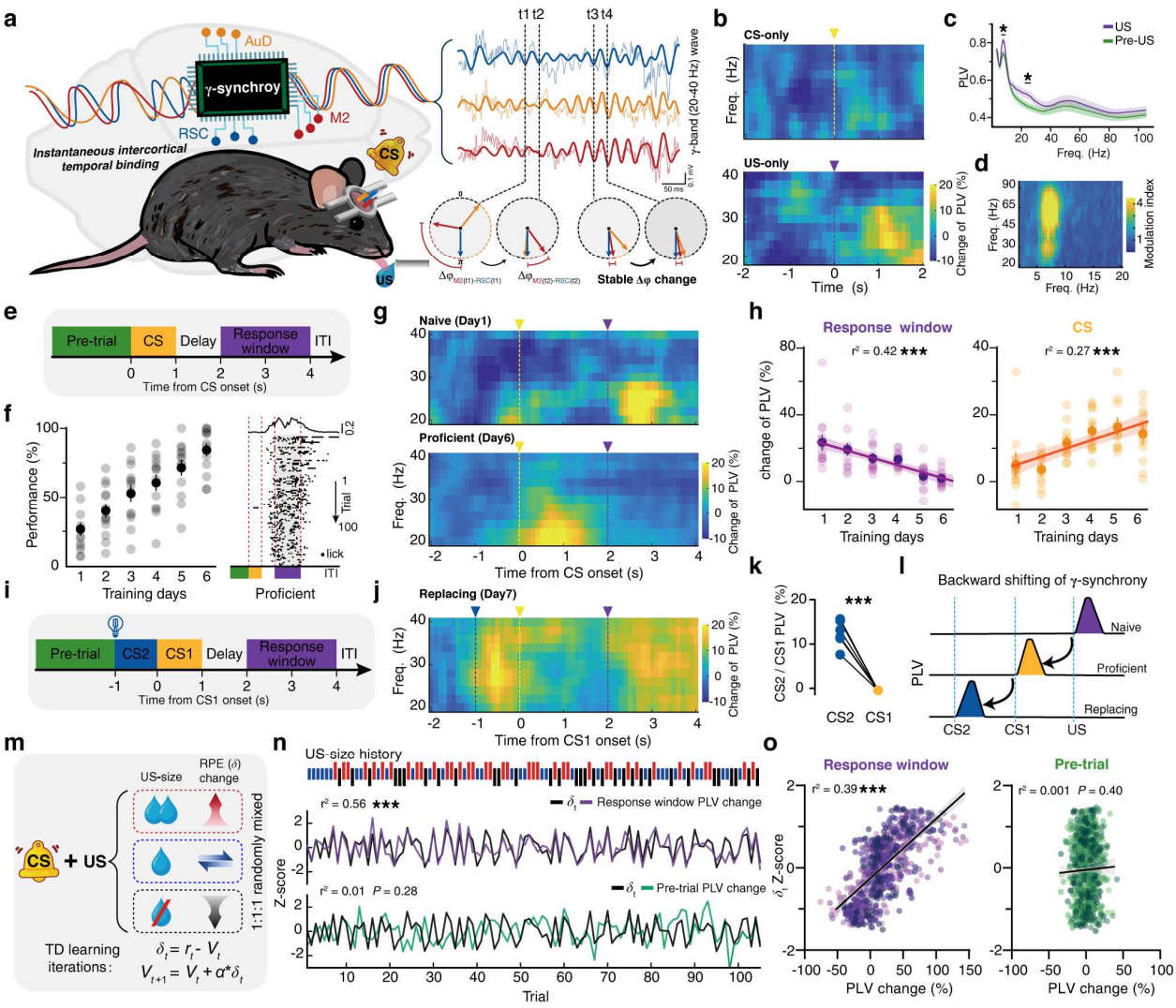

Fig. 1. Intercortical γ-synchrony dynamics conform to the TD learning algorithm.
(a) Left, schematic depiction of multi-region (RSC, AuD, M2) LFPs recording during a CS-US associative learning task. The hand-drawn mouse illustration is adapted from freepik.com. Right, representative γ-band (20–40 Hz, dark lines) phase extraction from LFP raw traces (tint lines). Phase locking value (PLV) is calculated by the difference (Δφ) between the instantaneous phases of the signals from these brain regions. The t1 and t2 time points are chosen from two consecutive RSC γ oscillation troughs, and the t3 and t4 time points are similarly chosen from two consecutive troughs in another time segment.
(b) Averaged γ-synchrony spectrogram for CS-only trials (top) and US-only trials (bottom), respectively. The spectrogram reflects the average of all 39 cortical pairs, including RSC-M2, RSC-AuD, and AuD-M2 from 13 mice. The triangle and dashed line indicate the onset times for CS (yellow) or US (purple) delivery.

(c) Comparison of the averaged overall synchrony in the US and pre-US time segments.
(d) Normalized phase-power modulation index comodulogram for US-only trials. The comodulogram is the average of all 39 cortical pairs within 2 seconds of the US onset time.
(e) Trial structure of CS-US associative training across day 1 to 6.
(f) Left, performance of all 13 mice. Right bottom, representative lick behavior of a proficient mouse (day 6). The density of licking actions was concentrated within the response window as learning progressed (right top).
(g) Spectrogram of averaged γ-synchrony for naive (top, day 1) and proficient trials (bottom, day 6). The triangle and dotted line indicate the onset time for CS (yellow) and the response window (purple).
(h) Linear regression of intercortical γ-synchrony within the response window (left, $r^2 = 0.42$, $P < 0.001$) and during a 1-second CS lasting period (right, $r^2 = 0.27$, $P < 0.001$), respectively. n = 13.
(i) Trial structure for CS replacing experiment on day 7.
(j) Spectrogram of averaged γ-synchrony for the CS replacing experiment (day 7, n = 6).
(k) Relative changes of averaged intercortical γ-synchrony during the CS2 period, normalized to the CS1 period.
(l) Diagram illustrating the backward shift of intercortical γ-synchrony accompanied by the RPE signal.
(m) Design of the trial-by-trial US size fluctuation experiment on day 7. Three trial types, including regular US size (blue), double US size (red), and US omission (black) trials, were randomly mixed in a 1:1:1 ratio.
(n) Top, representative reward history (bars in the same color coding as in M). Middle, a line diagram showing changes in PLV within the response window (purple), normalized to the baseline (averaged PLV within 6 seconds before CS), and trial-by-trial RPE value changes (black). Bottom, the changes in PLV within 2 seconds before CS (green), normalized to baseline, and trial-by-trial RPE value changes (black).
(o) Linear regression of trial-by-trial RPE value changes with intercortical γ-synchrony changes within the response window ($r^2 = 0.39$, $P < 0.001$, purple, n = 7) and within the last 2-second pre-trial period ($r^2 = 0.001$, green, n = 7).
$*P < 0.05$, $***P < 0.001$. *P* values were calculated using two-way ANOVA Sidak method (c), Pearson correlation test (h, n, and o), and two-tailed paired t test (k).

Main Figure 2

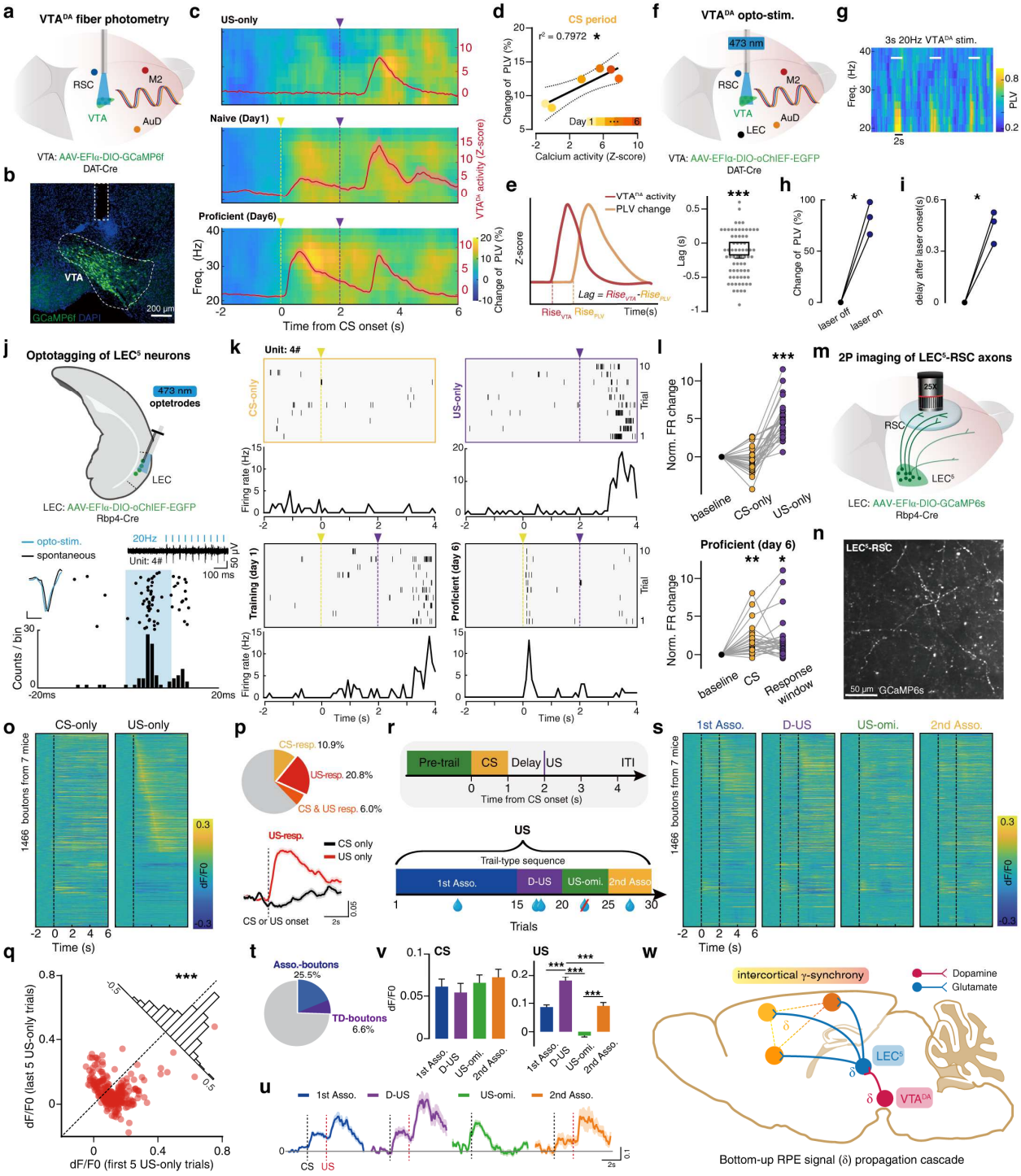

Fig. 2. The VTA^{DA}-LEC^{5} circuit transmits the RPE signal to the cortex.

(a) Viral strategy for expressing GCaMP6f in VTA^{DA} of DAT-Cre mice. Cortical LFPs were recorded simultaneously.

(b) Representative Cre-mediated expression of GCaMP6f in VTA^{DA} and optical fiber placement.
(c) One mouse example of trial-averaged intercortical γ-synchrony spectrograms with population activities of VTA^{DA} across different stages.
(d) Day-by-day correlation between trial-averaged population activity of VTA^{DA} and the changes in intercortical γ-synchrony within the CS period. n = 6.
(e) Left, method for calculating the time lag between VTA^{DA} calcium activity (red) and intercortical γ-synchrony (yellow) within the CS period. Right, quantification of time lags on day 6, compared to zero.
(f) Viral strategy for expressing oChIEF in VTA^{DA} of DAT-Cre mice. An optical fiber was implanted above the VTA. LFPs in LEC, RSC, M2, and AuD of the ipsilateral hemisphere were recorded.
(g) Spectrogram of intercortical γ-synchrony before and after optogenetic stimulation. White lines indicate laser stimuli. The spectrogram is an average of all cortical pairs, including RSC-M2, RSC-AuD, and AuD-M2.
(h) Quantification of PLV changes before and after optogenetics stimulation. n = 3.
(i) Time lags between the onset of the laser and PLV elevation. n = 3.
(j) Top, viral strategy for expressing oChIEF in LEC^5. Optetrodes were implanted in the LEC. Bottom, the averaged laser-evoked (blue) and spontaneous (black) spike waveforms of a representative single unit identified as Rbp4-positive neuron, along with peristimulus time histograms of 20 Hz laser pulse stimulation.
(k) Raster plots and firing rate changes of an example photoidentified LEC^5 neuron across different stages of associative learning. The triangle and dashed line indicate the start for CS (yellow) and the response window (purple).
(l) Top, relative changes in firing rates of all eleven photo-identified LEC^5 neurons in CS-only and US-only trials. Bottom, relative changes in their firing rates during the CS period and response window on the last day of training.
(m) Viral strategy for expressing GCaMP6s in LEC^5 of Rpb4-Cre mice. A cranial window over RSC was installed.
(n) Representative LEC^5-RSC axon boutons.
(o) Trial-averaged CS-only or US-only responses of LEC^5-RSC boutons (1466 boutons from 7 mice), sorted by the peak response time to US.
(p) Top, proportion of boutons that are CS-responsive, US-responsive, and co-responsive to both CS and US. Bottom, average calcium activities of the US-responsive group in response to either CS or US.
(q) Scatter plot of the average activities of US-responsive boutons during the first five and the last five US-only trials.
(r) Trial structure of CS-US training and design of the task including the first batch of 15 association trials with one drop of water (1st Asso.), followed by five double US trials with two drops of water (D-US) and five US omission trials without water delivery (US-omi.), then the second batch of five association trials with one drop of water (2nd Asso.).
(s) Trial-averaged responses of LEC^5-RSC boutons across different stages.

(t) Proportion of the CS-US association responsive group and the group that meets the TD learning model (TD-boutons).
(u) Averaged responses of all 97 TD-boutons (n = 7) to four trial types.
(v) Quantification of averaged responses within the CS period (left) or within 2 seconds after US delivery (right) of TD-boutons to all four trial types.
(w) Flatmap summary of the bottom-up RPE signal propagation cascade.
**P* <0.05, ***P* <0.01, ****P* <0.001. *P* values were calculated using two-tailed paired t test (e, h, and i), Pearson correlation test (d), Kolmogorov-Smirnov test (q), and one-way ANOVA Tukey test (l and v).

Main Figure 3

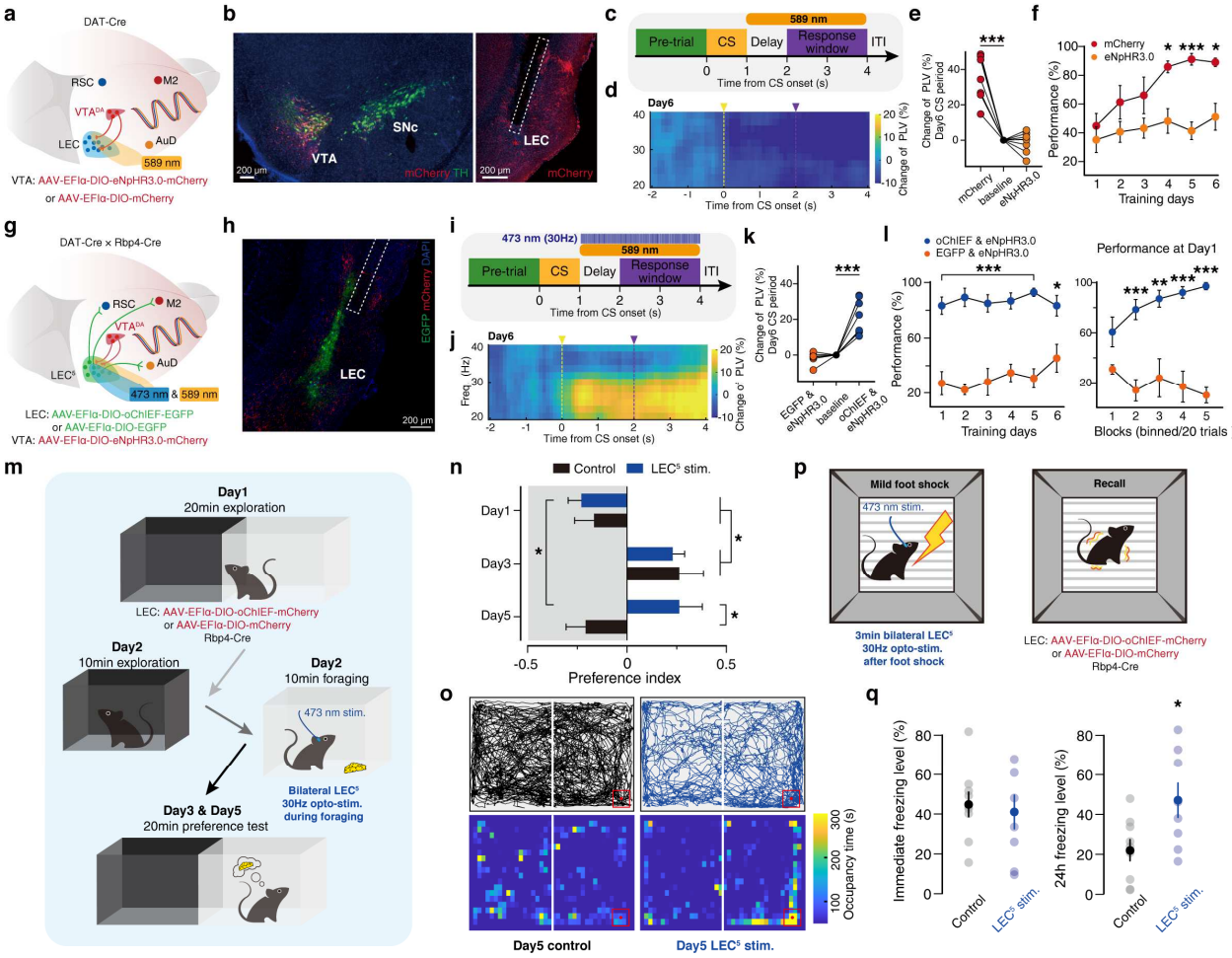

Fig. 3. Facilitation of learning and memory retention through the manipulation of the VTA^{DA}-LEC^{5} circuit.

(a) Viral strategy for the bilateral expression of eNpHR3.0-mCherry or mCherry in VTA^{DA} of DAT-Cre mice. Optical fiber cannulas were bilaterally implanted above the LEC.

(b) Left, representative Cre-mediated expression of eNpHR3.0-mCherry in VTA^{DA}. Dopamine neurons were stained with Tyrosine Hydroxylase (TH) antibody in both VTA and substantia nigra pars compacta (SNc). Right, representative VTA^{DA} axons transfected with eNpHR3.0-mCherry and optical fiber placement.

(c) Trial structure of CS-US training from day 1 to day 6. In each trial, a 589 nm laser was applied continuously for 3 seconds, covering both the delay period and the response window.

(d) Trial-averaged intercortical γ-synchrony spectrogram of one mouse example from the inhibition group on day 6.

(e) Quantification of the relative changes in averaged PLV within the CS period in the mCherry control group (n = 7) and the inhibition group (n = 8). Compared to each of their respective average baseline PLV (within 2 seconds before CS).

(f) Performance of the mCherry control group (n = 7) and the inhibition group (n = 8) across six training days.
(g) Viral strategy for the bilateral expression of eNpHR3.0-mCherry in VTA^{DA} and oChIEF-EGFP or EGFP in LEC^{5} in DAT-Cre × Rpb4-Cre mice. Two optical fibers were bilaterally implanted above the LEC.
(h) Representative Cre-mediated expression of eNpHR3.0-mCherry in VTA^{DA} axons and oChIEF-EGFP in LEC^{5}.
(i) Trial structure of CS-US training. In each trial, a 589 nm (constant) and a 473 nm (30 Hz) hybrid laser were applied simultaneously for 3 seconds, covering the delay period and response window.
(j) Trial-averaged intercortical γ-synchrony spectrogram of one mouse example from the oChIEF & eNpHR3.0 group on day 6.
(k) Quantification of the relative changes in averaged PLV within the CS period in the EGFP & eNpHR3.0 control group (n = 6) and the oChIEF & eNpHR3.0 group (n = 7), compared to their respective averaged baseline PLV (within 2 seconds before CS onset).
(l) Performance of the EGFP & eNpHR3.0 control group (n = 6) and the oChIEF & eNpHR3.0 group (n = 7) over six training days (left) and five blocks on day 1 (right).
(m) Procedures of the CPP experiment.
(n) Quantification of the preference index for the two groups of mice.
(o) Representative exploration trajectory (top) and occupancy map (bottom) during memory recall on day 5 for the control group and LEC^{5} stimulation group (right), respectively.
(p) Paradigm of CFC training and recall tests. Mice received a mild electric foot shock (0.3 mA, 2 seconds) during CFC training. The freezing levels were measured twice: once immediately after the training and again 24 hours later.
(q) Quantification of the freezing levels in the mCherry control group (n = 9) and the oChIEF group (n = 8) for immediate recall (left) and 24-hour recall (right), respectively.
$*P < 0.05$, $**P < 0.01$, $***P < 0.001$. *P* values were calculated using two-tailed t test (q), two-tailed paired t test (e and k), two-way ANOVA Tukey test (n), and multiple t tests Holm-Sidak method (f and l).

Main Figure 4

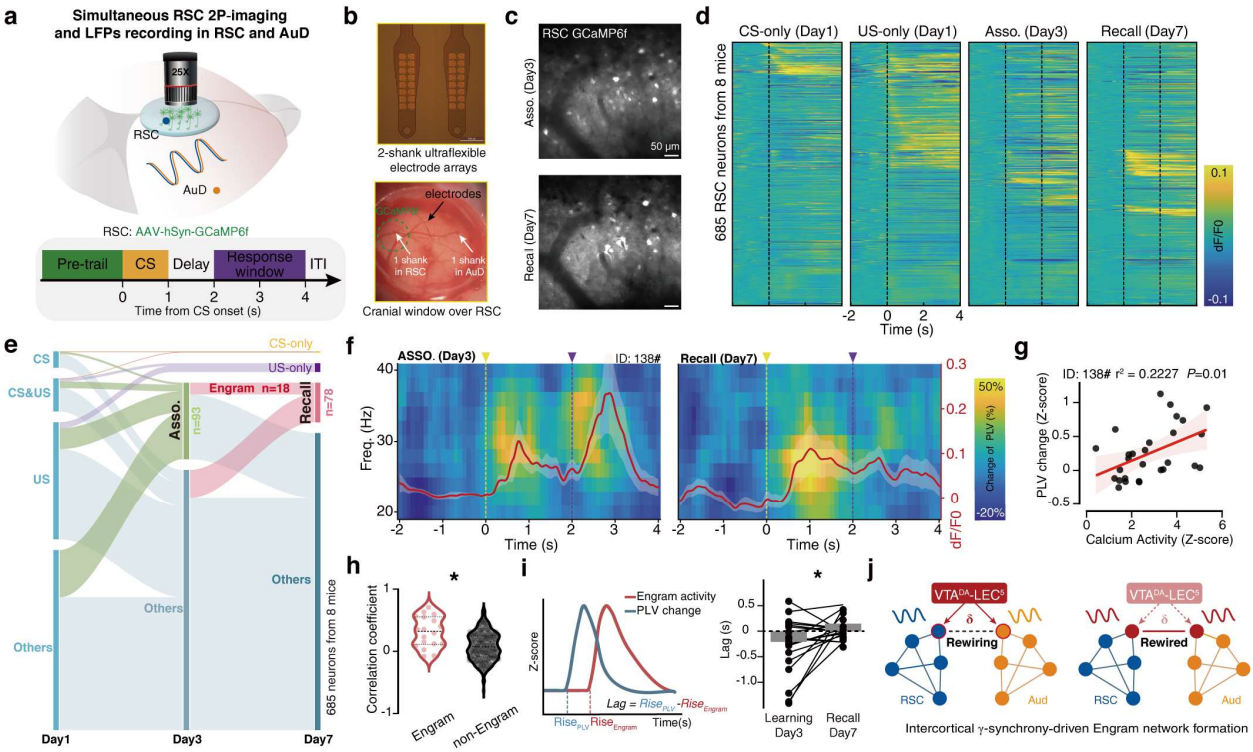

Fig. 4. Intercortical γ-synchrony entrains the activity of RSC latent Engrams.
(a) Top, viral strategy for expressing GCaMP6f in RSC. LFPs in RSC and AuD were recorded simultaneously. Bottom, trial structure of CS-US training and recall test from day 1 to day 7.
(b) Top, a microscopic image of 2-shank ultraflexible electrode arrays. Bottom, a photograph of a 5 mm wide cranial window over the RSC virus injection region (highlighted in green) and the ultraflexible electrode arrays implanted within the RSC and AuD.
(c) Representative 2P field of view during training (top) and recall (bottom).
(d) Trial-averaged activities of all 685 neurons (n = 8) across different stages, sorted by response to CS-only, US-only, association training (day 3), and memory recall (day 7) in succession.
(e) An alluvial diagram illustrating the grouping trends of response characteristics across different stages for all neurons.
(f) Averaged RSC-AuD γ-synchrony spectrogram with activity of one example RSC latent Engram during learning (left) and recall (right).
(g) Trial-by-trial correlation between calcium activity of a representative latent Engram (same neuron in f) and the change in intercortical γ-synchrony during learning on day 3.
(h) Quantification of the trial-by-trial correlation coefficient between changes in intercortical γ-synchrony and calcium activity in each latent Engram or the remaining non-Engram neurons.
(i) Left, method for calculating the rising time lags between intercortical γ-synchrony (blue) and calcium activity of the latent Engram (red). Right, quantification of time lags during learning (day 3) and recall (day 7), respectively.

(j) Diagram summarizing the underlying mechanism of intercortical γ-synchrony involved in RPE signal propagation and cortical Engram network formation.
*P <0.05. P values were calculated using the Pearson correlation test (g), Kolmogorov-Smirnov test (h), and two-tailed paired t test (i).

Main Figure 5

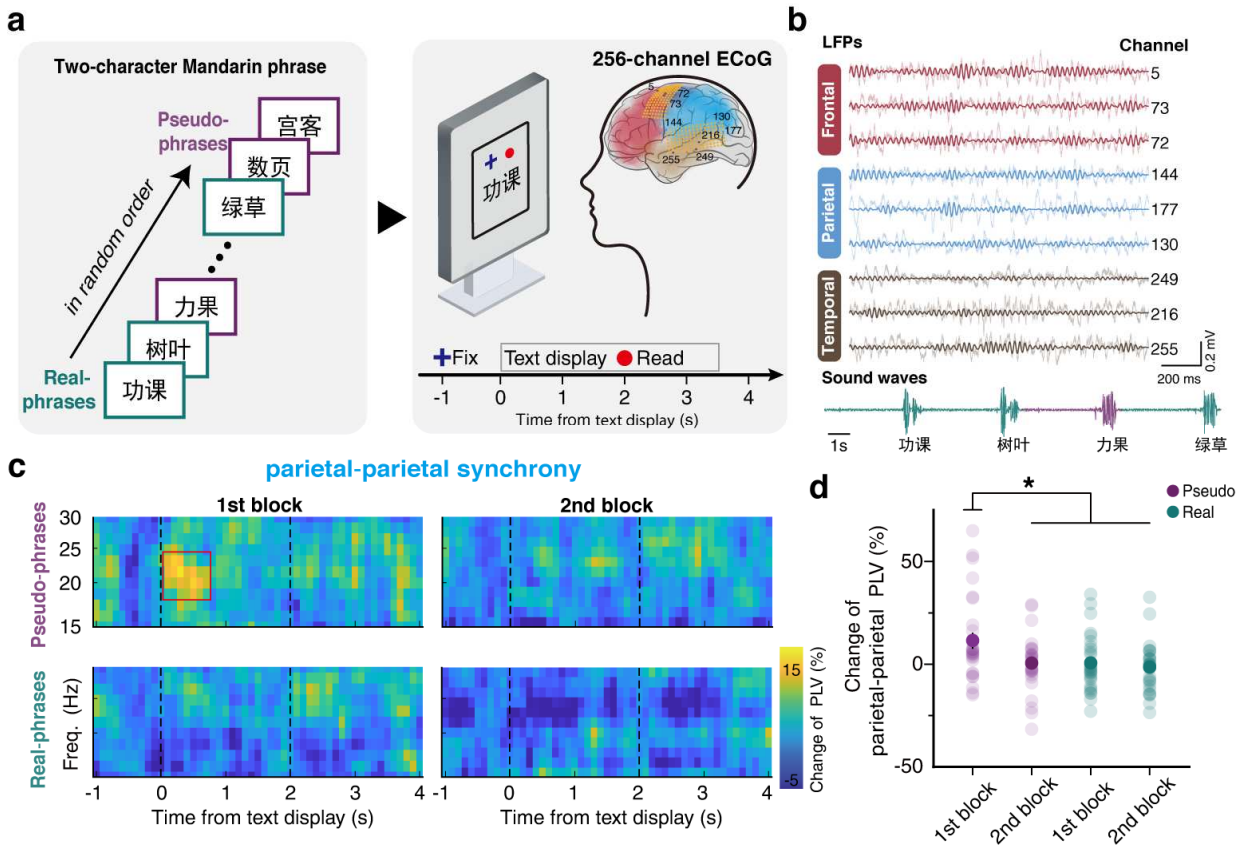

Fig. 5. Unexpected pseudo-phrases sensitive γ-synchrony in the human brain.
(a) Left, two-character Mandarin pseudo-phrases (purple) and real-phrases (green) were presented to the subject in a random order. An experiment with two blocks was carried out, with three appearances for each phrase in each block. Right, in each trial, a warning sign prompting the subject to concentrate appears for 1 second, followed by a 2-second text display period, and then a reminder to start reading. Each subject used two 128-channel ECoG electrode arrays covering major areas, including the frontal lobe, temporal lobe, and parietal lobe.
(b) Representative gamma band (20–40 Hz, dark lines) waves extracted from ECoG raw traces (tint lines) in the frontal lobe (red), parietal lobe (blue), and temporal lobe (brown), respectively. Sound waves were recorded to verify an accurate reading.
(c) Spectrograms of averaged parietal-parietal γ-synchrony for pseudo-phrases (top) and real-phrases (bottom) during the 1st block (left) or 2nd block (right), respectively (28 pairs from 7 patients). The red box marks the time and frequency range of significant change.
(d) Quantification of parietal-parietal γ-synchrony within 1 second after the text display. **P* <0.05. *P* values were calculated using one-way ANOVA Tukey test.

Materials and methods

Mice

All mice were housed in the Animal Core Facility at ShanghaiTech University and kept on a 12-hour light/dark cycle with free access to food and water. The facility maintained a steady temperature of 22–26°C, relative humidity between 40% and 70%, and noise levels below 60 dB. Both male and female mice aged 4–6 months were used. C57BL/6J mice were purchased from Shanghai Jihui Laboratory Animal Care. The Rbp4-Cre (MMRRC, Stock No. 031125-UCD) line was obtained from the Mutant Mouse Resource & Research Centers (MMRRC). The Ai9 (JAX, Stock No. 007909) line was obtained from the Jackson Laboratory. The DAT-Cre (JAX, Stock No. 006660) line was kindly provided by Dr. Ji Hu (ShanghaiTech University). To generate DAT-Cre × Rbp4-Cre double-transgenic mice, the DAT-Cre line was bred with the Rbp4-Cre line. All animal experiments were conducted in accordance with protocols approved by the Institutional Animal Care and Use Committee of ShanghaiTech University.

Stereotaxic surgery

Mice were anesthetized with 5% isoflurane for induction and placed in a stereotaxic apparatus (RWD Life Science Co., Ltd., China), where they were maintained under 1% isoflurane anesthesia. The scalp was disinfected with povidone-iodine, shaved, and incised to expose the skull. The soft tissue above was carefully removed, and the skull was precisely leveled by ensuring the Bregma and Lambda points were aligned on the same dorsal-ventral plane for further procedures. All coordinates are provided relative to Bregma. For simplicity, all injection or implantation coordinates used in the following experiments are listed here: RSC (AP: −3.0 mm, ML: −0.5 mm, DV: −0.3 mm); M2 (AP: −1.0 mm, ML: −1.0 mm, DV: −0.3 mm); AuD (AP: −3.0 mm, ML: −4.0 mm, DV: −0.3 mm); VTA (AP: −3.08 mm, ML: −0.6 mm, DV: −4.5 mm); LEC (AP: −4.0 mm, ML: −4.2 mm, DV: −4.2 mm). All the viruses (titers varied from 1 to 2×10^{13} ml^{-1}) were purchased from Obio Technology (Shanghai) Co., Ltd. A glass pipette (Wiretreol II 5 and 10, Drummond) was beveled at a 45-degree angle and filled with mineral oil; it was subsequently connected to an automated hydraulic pump (RWD Life Science Co., Ltd., China) for virus injection. Optical fibers (200 μm core diameter, NA 0.37, HealthiGlobal Tech Co., Ltd., China) were employed for fiber photometry or optogenetics manipulation experiments. In experiments involving head-fixed mice, all implants and a custom-designed titanium head-plate were affixed to the skull using dental cement. Postoperative recovery for the mice was conducted on a heated platform until they exhibited normal behavior. Within one week, they were provided with fortified nutritional jelly containing the analgesic carprofen (5 mg). A minimum duration of two weeks was designated for recovery before advancing to any subsequent phase of the experiment.

For multi-site electrode implantation, custom-made electrodes with PFA-coated tungsten wires (A-M Systems, 795500) were used to record LFPs. Only electrodes with an impedance below 2 MΩ were employed. Craniotomies were performed at RSC, AuD, and M2, followed by stereotaxic implantation. Two skull screws were implanted over the cerebellum, one acting as a reference electrode and the other as a ground electrode.

For the fiber photometry experiment, AAV9-EF1α-DIO-GCaMP6f (150 nL) was injected into the unilateral VTA of DAT-Cre mice at a rate of 50 nL/min. After the injection, an optical fiber was implanted above the injection site. The procedure for tungsten electrode implantation and the recording coordinates in RSC, AuD, and M2 were consistent with those described above.

For the optogenetic stimulation of the VTA^{DA} experiment, a separate group of DAT-Cre mice was injected with AAV9-EF1α-DIO-oChIEF-EGFP (150 nL) into the unilateral VTA. In addition to RSC, AUD, and M2, a tungsten electrode was also implanted in the ipsilateral LEC. The procedures for implanting the tungsten electrode and optical fiber were consistent with those described above.

For the optogenetic tagging experiment, AAV9-EF1α-DIO-oChIEF-EGFP (150 nL) was injected into the unilateral LEC^5 of Rbp4-Cre mice. Subsequently, four skull screws were attached, with one serving as a ground and another as a reference. A 32-channel optetrode array, assembled from one optical fiber and eight tetrodes arranged in a 2×4 configuration, spaced 150 μm apart (KedouBC, China), was then angled laterally at 10 degrees and inserted at the LEC^5 injection site. The exposed cortical surface was carefully covered with surgical silicone adhesive (Kwik-Sil, World Precision Instruments, USA).

For the anterograde trans-synaptic tracing experiment, AAV1-hSyn-Cre (150 nL per hemisphere) was injected into the bilateral LEC of Ai9 mice.

For the optogenetic inhibition of the VTA^{DA}-LEC^5 experiment, AAV9-EF1α-DIO-eNpHR3.0-mCherry (150 nL per hemisphere) or AAV9-EF1α-DIO-mCherry (150 nL per hemisphere) was injected into the bilateral VTA of DAT-Cre mice. Subsequently, two optical fibers were bilaterally implanted above the LEC. Tungsten electrodes were also implanted in the RSC, AuD, and M2 areas of the right hemisphere.

For the combined optogenetic inhibition of the VTA^{DA}-LEC^5 pathway and stimulation of the LEC^5 experiment, AAV9-EF1α-DIO-eNpHR3.0-mCherry (150 nL per hemisphere) was bilaterally injected into the VTA of DAT-Cre × Rbp4-Cre mice. Additionally, bilateral LEC^5 were injected with either AAV9-EF1α-DIO-oChIEF-EGFP (150 nL per hemisphere) or AAV9-EF1α-DIO-EGFP (150 nL per hemisphere). Subsequently, two optical fibers were implanted bilaterally above the LEC. Tungsten electrodes were also implanted in the RSC, AuD, and M2 area of the right hemisphere.

For the CPP and CFC experiments, Rbp4-Cre mice received bilateral injections into LEC^5 of either AAV9-EF1a-DIO-oChIEF-mCherry (150 nL per hemisphere) or AAV9-EF1a-DIO-mCherry (150 nL per hemisphere). After the injections, two optical fibers were implanted bilaterally above the LEC^5.

For 2P imaging of LEC^5-RSC axons, AAV9-EF1α-DIO-GCaMP6s (150 nL) was injected into the unilateral LEC^5 of Rbp4-Cre mice. A 4–5 mm circular craniotomy was performed centered on the RSC using a high-speed drill and a dissecting microscope for visualization. Subsequently, the craniotomy was sealed with a 5-mm-diameter glass coverslip (World Precision Instruments, USA). 2P calcium imaging was performed one month after the surgery.

For simultaneous 2P imaging of RSC neurons and LFP recording in the RSC and AuD, a 4–5 mm circular craniotomy was performed over both regions. An injection of AAV9-EF1α-GCaMP6f (150 nL) was delivered into the RSC at a depth of 300 μm below the pial surface. Next,

the 2-shank ultraflexible electrode arrays were implanted in both the RSC and AuD (n = 4). The design and configuration of the 2-shank ultraflexible electrode arrays are shown in Extended Data Fig. 7a. The implantation procedure adhered to protocols described in the literature[51]. For mice using tungsten electrodes to record LFPs from the superficial layers of the RSC and AuD (n = 4), ultra-fine tungsten wires (PTFE-coated, 20 μm in diameter, California Fine Wire, 100211) were manually bent into electrodes approximately 0.3 mm long and inserted into the cortex as shown in Extended Data Fig. 7c. The craniotomy was then sealed with a 5-mm-diameter glass coverslip. 2P calcium imaging was conducted at least one month after surgery.

Human participants

This study involved seven native Mandarin speakers (five males and two females; aged 25–60 years) with left-hemisphere language dominance who underwent awake brain tumor resection with language mapping at Huashan Hospital, Shanghai, China. All participants were clinically indicated for awake surgery. High-density electrocorticography (ECoG) grids were placed intraoperatively over the temporal, frontal, and parietal cortices to record local field potentials (Extended Data Fig. 8 and Extended Table 3). The grid was positioned by an experienced neurosurgeon, guided by clinical expertise and the necessity to avoid the tumor. The study was approved by the Institutional Review Board (IRB) of Fudan University Huashan Hospital (HIRB KY2019-538) and conducted in strict compliance with ethical standards. All participants were informed of the voluntary nature of the study and their right to withdraw at any point, and written consent was obtained from each.

The pial surfaces were reconstructed from preoperative T1-weighted MRI scans using FreeSurfer (v7.2.0). The intraoperative localization of electrode grids was assisted by the Medtronic StealthStation S7 neuronavigation system, which recorded the three-dimensional coordinates of the grid corners. These fiducial markers were aligned to the preoperative MRI space, supplemented by intraoperative photographs for spatial validation. The remaining electrode centroids were calculated with the Python "img_pipe" package (v1.3), which uses geodesic interpolation algorithms based on the established corner coordinates. All electrode positions were normalized to the MNI 152 asymmetric template (2009 release) through nonlinear volumetric registration. Anatomical labeling assigned each electrode to a specific cortical region according to the Desikan-Killiany atlas.

CS-US associative learning

Mice were subjected to a water-restricted diet to maintain their body weight at 80–85% of their initial weight. Training started once their weight reached 85%. They were monitored daily for overall health during the experiment. Mice were head-fixed in a custom frame for training. The day before training, a shaping session was conducted, during which mice received 10 CS-only (2 kHz tone) trials and 10 US-only (one drop of water, ~7 μL) trials, delivered separately with a randomized 5–8 s inter-trial interval (ITI). Afterwards, mice performed the CS-US associative learning task (100 trials per day). Each trial included a 4–6 s lick withhold period, a 1 s CS delivery, a 1 s delay, and a 2 s response window. Only licking the water pipe within the response window

activates the infrared sensor to dispense a drop of water as a reward. The ITI duration is randomly set between 5 and 8 seconds.

The CS replacing experiment was conducted on day 7 with six proficient mice from the earlier CS-US association training. In this experiment, a blue light cue was presented 1 second before the tone cue (Fig. 1i).

For the US-size fluctuation experiment, the CS-US contingency was adjusted by randomly changing the US size in each trial on day 7 for the other seven proficient mice (Fig. 1m). The trial structure followed the standard CS-US task, except that the US size during the response window varied across three trial types: US-omission (no reward), regular US size with one drop of water (~7 μL), and double US size with two drops of water (~14 μL). A total of 120 trials were conducted in a 1:1:1 randomized ratio. The trial-by-trial relative changes in RPE values after delivering different rewards to mice were calculated using the TD learning iterative algorithms. Trials where animals did not water-lick at all from CS to ITI were excluded, as these trials indicated incomplete engagement with the environment. The initial expectation of reward ($V1$) for each mouse was set to its hit rate on day 6, with a learning rate (α) of 0.5. The outcome (r_t) for different US sizes in each trial was assigned a value of 1.5 for two drops of water, 1 for one drop of water, and 0 for reward omission.

The CS-US associative learning task was performed in a custom-made behavioral box controlled by an Arduino microcontroller. The interior surfaces of the box are covered with sound-absorbing foam to reduce environmental noise. In addition to an infrared video camera that monitored animal behavior, an infrared photobeam sensor provided millisecond-precise detection and timing of licking events. Performance for each mouse was assessed as the fraction of rewarded trials out of all training trials completed that day. The behavioral data were hardware-synchronized with electrophysiology recording, fiber photometry, and 2P imaging.

LFPs recording and analysis

The multi-channel data were collected and amplified using an Apollo neural data acquisition system (v1.0, Bio-Signal Technologies, USA). The inner walls of the behavioral box were lined with a continuous copper mesh connected to ground to shield against electromagnetic interference. LFPs were recorded at 1 kHz and digitally stored after online band-pass filtering between 1 and 200 Hz. Unless stated otherwise, all analyses were conducted with custom MATLAB scripts. Before further analysis, channels with low signal-to-noise ratios (SNR) were identified and excluded. Causes of low SNR included 50 Hz power-line interference, electromagnetic noise from nearby equipment, and poor contact between the recording screw and cortical tissue. Power-line artifacts were reduced using the rmlinesc function from the Chronux toolbox (https://chronux.org). Zero-phase band-pass filtering was performed using MATLAB-designed IIR filters combined with the built-in filtfilt function. LFP analyses in this study focused on three metrics: LFP power, phase-amplitude coupling (PAC) across frequencies, and long-range phase synchrony. To estimate LFP power, spectral power was calculated using the mtspecgramc function in the Chronux toolbox and then converted to decibels (dB) for visualization. PAC strength was measured with an optimized version of the modulation index (MI) developed by Tort et al.[52]. To examine dynamic changes in neural synchrony, we adapted methods from Lachaux et al. to compute the theta-coupled phase-

locking value (PLV) between brain regions[17,53]. For each trial, LFP signals were transformed into the time-frequency domain using the Morlet wavelet transform, and PLV was calculated with a sliding window (window size: 1 s, step size: 0.1 s). Within each window, PLV was calculated as follows:

$$PLV_{(f,t)} = \left|\frac{1}{n}\sum_{k=1}^{n} e^{i(P_{electrod1}(f,k)-P_{electrode2}(f,k))}\right| \quad (1)$$

where f is frequency, t is the center time point of the window, n is the number of samples within the window, k is the sample index, and $P_{electrod1}$ and $P_{electrod2}$ represent the instantaneous phases of the signals from the two electrodes at frequency f and time t, respectively. For optogenetic tagging, the same system was configured to record at a rate of 30 kHz.

Fiber photometry

Fiber photometry was conducted using a commercial Fiber photometry DAQ system (QAXK-FPS-LASER, Thinker Tech, China). A 488 nm laser, with a power of less than 45 μW at the fiber tip, was used. To prevent photobleaching, recordings were limited to 15 minutes per mouse per day. Signals were sampled at 100 Hz. To ensure consistency in data processing across training days, we analyzed only the signals from hit trials. The dataset, collected from day 1 to day 6 of training, included 200 trials from six mice. Data were processed offline with custom MATLAB scripts. For each trial, signals were baseline Z-scored to the 2-second pre-stimulus period. To quantify the relationship between γ-synchrony and VTA^{DA} neuron activity, fiber-photometry traces were downsampled to 10 Hz to match the temporal resolution of the PLV. 20–40 Hz PLV was averaged, and within the stimulus epoch, we extracted the maximum PLV and the maximum photometry amplitude. Daily mean signal amplitudes were then used to assess the linear correlation between PLV and photometry activity. To compare response onset latencies of γ-synchrony and VTA^{DA} neuron responses to external stimuli, the response onset index for each trial was computed using MATLAB's built-in function gradient, and the latency difference between the two signals was defined as Lag = Time $_{\text{max gradient VTA}}$ - Time $_{\text{max gradient PLV}}$.

Optogenetic manipulation

A 470 nm laser (Lasever, China) was used for optogenetic activation, and a 589 nm laser (Lasever, China) was used for optogenetic inhibition. The timing of laser application was precisely controlled by a custom-made, Arduino-based circuit. For activating VTA^{DA} neurons, a 470 nm laser (7 mW/mm² at the fiber tip, 20 Hz pulse train, 10 ms per pulse) was applied. For optotagging LEC^5 neurons, a 470 nm laser (5 mW/mm² at the fiber tip, 20 Hz pulse train, 10 ms per pulse) was used. To inhibit VTA^{DA}-LEC^5 axons during the CS-US associative learning task, a constant 589 nm laser (7 mW/mm² at the fiber tip) was applied in each trial for 3 seconds, covering the delay period and response window. For simultaneous inhibition of VTA^{DA}-LEC^5 axons and stimulation of LEC^5 neurons, 589 nm (7 mW/mm² at the fiber tip, constant) and 473 nm (7 mW/mm² at the fiber tip, 30 Hz pulse train, 10 ms per pulse) lasers were combined using a 2×2, 50:50 multi-mode

fiber coupler (TT200FL2A, Thorlabs, USA). These hybrid lasers were applied together for 3 seconds, covering the delay period and response window. For the CPP experiment, a 473 nm laser (7 mW/mm² at the fiber tip, 30 Hz pulse train, 10 ms per pulse) was used for 10 minutes to activate LEC^5 neurons. For the CFC experiment, the same 473 nm laser (7 mW/mm² at the fiber tip, 30 Hz pulse train, 10 ms per pulse) was used for 3 minutes to activate LEC^5 neurons.

Optotagging and spike sorting

All optotagging and spike recordings were performed with an Apollo system (v1.0, Bio-Signal Technologies, USA). The raw signals were processed through a preamplifier to distinguish spike activities (using a 300 Hz high-pass filter, sampled at 30 kHz) and LFPs (using a 200 Hz low-pass filter, sampled at 1 kHz). Before each recording session, 20 Hz blue laser trains lasting 1 second were delivered to identify oChIEF-expressing units. A unit was classified as an Rbp4-positive neuron if it showed high reliability of laser-evoked spikes with a short latency (<10 ms). We further confirmed their identity by comparing waveform correlations between laser-evoked and spontaneous spikes. A total of 11 Rbp4-positive neurons were isolated from six mice, with most recorded from a single tetrode. Spike sorting was done manually using Plexon Offline Sorter (version 4.5.0) and MATLAB scripts from https://github.com/MathWorks-Teaching-Resources/Electrophysiology-Tutorial-for-Neuroscience/releases/tag/v1.2. Mean spike activity was averaged in 100-ms bins. The circular vector length, used to measure the degree of spike-oscillation phase locking, was calculated following the method described in the literature[54].

2P calcium imaging

During the CS-US associative learning task, calcium imaging was performed in awake, head-fixed mice using a two-photon microscope (25× water-immersion objective, NA 1.05, FVMPE-RS, Olympus, Japan) as previously described[55]. The excitation wavelength was 960 nm (Ti: sapphire, approximately 10 mW at the brain, held constant). Emission was collected at 380–480, 500–540, and 560–650 nm. The field of view measured 509 × 509 μm. Imaging was captured at 30 frames per second (fps).

For 2P imaging of RSC neurons, to minimize GCaMP6f photobleaching artifacts, imaging sessions were conducted only on day 1 (10 trials each for CS-only and US-only), day 3 (30 CS-US trials), and day 7 (30 CS-US trials). On the remaining days, the mice underwent only 100 CS-US training trials without 2P imaging. For 2P imaging of LEC^5-RSC axons, due to the low photostability of untargeted axonal GCaMP6s and the difficulty of maintaining the same field of view across days, the response window was replaced with direct reward delivery (exemption from triggering) to speed up the imaging process. Mice first completed ten trials each of CS-only and US-only stimuli, followed by a training session consisting of a batch of 15 association trials with one drop of water (1st Asso.), five double US trials with two drops of water (D-US), and five US omission trials without water delivery (US-omi.). Then, a second batch of five association trials with one drop of water (2nd Asso.) was conducted. The noise suppression DeepCAD-RT approach was used for both RSC neurons and LEC^5-RSC axons (https://github.com/cabooster/DeepCAD-RT)[56].

Conditioned Place Preference (CPP)

Mice were kept on a food-restricted diet throughout the entire experiment to maintain a body weight of 80–85%. Training started when the body weight reached 85%. The mice were monitored daily for general health. Behavioral testing was conducted in a custom two-chamber box (60 × 40 cm) with a removable divider that allowed for either connection or separation of the compartments. One compartment had black interior walls (the dark box), while the other had white interior walls (the light box). On the first day, mice were gently placed at the junction between the two compartments and allowed to explore both sides for 20 minutes. Baseline exploration showed a spontaneous preference for the dark compartment. On the second day, the compartments were separated with the divider. Mice first experienced a 10-minute exploration in the dark box without buried food or optogenetic stimulation, followed by a 10-minute foraging period in the bright box containing buried food. During foraging, bilateral LEC^5 neurons were stimulated with a 473 nm laser pulsed at 30 Hz (other optical parameters as specified in the *Optogenetic manipulation* section). During the recall tests on days 3 and 5, with the divider removed, mice were gently placed at the compartment boundary and allowed to explore both sides for 20 minutes without buried food and without optogenetic stimulation. The time spent in each compartment was measured to assess the preference index. A ceiling-mounted camera (Logitech) recorded the mice's trajectories with high spatial and temporal resolution (30 frames per second). Behavioral trajectories were analyzed offline from video recordings using custom MATLAB scripts, and the duration of occupancy within each compartment was quantified. During the CPP task, a preference index was calculated for each mouse as $(Time_{light} - Time_{dark}) / (Time_{light} + Time_{dark})$ and summarized at the group level.

Contextual Fear Conditioning (CFC)

Experiments were carried out using the Multi Conditioning System (version 2.0, TSE Systems, Germany). During the conditioning session, mice were placed in the conditioning chamber (20 × 20 cm) and allowed to habituate for 3 minutes before receiving a mild foot shock (0.3 mA for 2 seconds). Immediately afterward, LEC^5 neurons were subjected to optogenetic stimulation with a 470 nm laser pulsed at 30 Hz for three minutes (other optical parameters as specified in the Optogenetics section). Freezing behavior was measured during two recall tests, each lasting three minutes, conducted immediately after conditioning and 24 hours later. For the CFC task, animal behaviors were automatically recorded by the TSE Multi Conditioning System. The freezing level was assessed using the system's built-in analysis software, which employed the manufacturer's default freezing-detection algorithm with a minimum bout duration of one second. The results were then exported for further analysis. For each mouse, the freezing percentage was calculated as the proportion of time classified as freezing during the recall test.

Mandarin phrase-reading task

Each patient undergoing awake glioma resection participated in a two-character Mandarin phrase-reading task. Each trial had three sequential phases: an initial 1-second fixation period with a central crosshair displayed, followed by a 2-second perception phase during which Mandarin lexical stimuli appeared in green, and finally a 1.5-second production phase. At the start of the production phase, the stimulus color changed from green to red, prompting participants to vocalize

the displayed text. The stimulation included four real phrases and four pseudo-phrases. Each phrase was presented in sessions of three repetitions, with each session consisting of two blocks and a few-minute rest between sessions, resulting in six total repetitions per phrase.

ECoG signals were recorded at a sampling rate of 3,052 Hz using Tucker-Davis Technologies (TDT) multichannel amplifiers integrated with digital acquisition systems. The timing of visual stimuli was precisely synchronized using photodiode monitoring of the presentation screen, and this information was directly fed into the TDT circuitry to ensure accurate alignment with the ECoG data. Online referencing was performed with a skull electrode placed at the Cz location, and no additional re-referencing was done during acquisition. Due to variability in electrode placement across patients, all electrode channels were first classified into three groups based on their anatomical location: frontal, temporal, and parietal. Before proceeding with further analysis, channels with issues were identified and excluded from the dataset. To handle the high dimensionality and computational demands of the PLV analysis, a subset of nine channels per patient was selected (Extended Data Fig. 8 and Extended Table 4). Specifically, three spatially distant electrodes were randomly chosen from each of the three anatomical regions, ensuring a uniform and random distribution across the recorded lobes. Raw data from these channels were downsampled to 1 kHz, and power-line noise was filtered out. Time-frequency analysis was then conducted using the Chronux toolbox (version 2.12), and PLV was calculated for each trial according to Equation (1). For the statistical analysis, PLV values from all trials were first averaged for each experimental block and for each phrase, respectively. This averaging was performed within the 20–25 Hz frequency band and the 0.4–0.6 second window following phrase onset. The mean PLV values were then compared using a paired one-way ANOVA, followed by post-hoc tests for multiple comparisons.

Histology

Mice were anesthetized with 3% tribromoethanol and perfused with PBS, followed by 4% paraformaldehyde (PFA, 158127, Sigma-Aldrich) in PBS. Brain tissue was post-fixed overnight. Coronal brain sections (50 μm thick) were cut using a Leica vibratome (VT1000 S). For staining, sections were first washed three times with PBS and then blocked in a solution of 10% goat serum (EE0008, SparkJade, China) in PBS for 30 minutes at room temperature. Next, the sections were incubated overnight at 4°C with a primary antibody. After three washes, the sections were incubated for 1 hour at room temperature with a secondary antibody. The antibodies used in the experiment are listed in Table S2. All antibodies were used at a dilution of 1:1000. After three additional washes, the sections were coverslipped using Fluoromount-G with DAPI (36308ES20, Yeasen, China). All samples were imaged on a spinning disk confocal microscope (Nikon CSU-W1, Nikon, Japan) using a 20×/0.75 objective. The animals used in the recording experiments were sacrificed to verify the position of the implants or the areas of virus infection.

Statistical analyses

Data are shown as mean ± SEM. Statistical analyses were performed in GraphPad Prism (v9.0.0, GraphPad Software) and MATLAB (2020b). Two-tailed paired or unpaired t test, multiple t tests, one-way ANOVA, two-way ANOVA, and the Kolmogorov-Smirnov test were used as

appropriate. The significance threshold was set at $P < 0.05$. Significance is denoted as follows: *$P < 0.05$, **$P < 0.01$, ***$P < 0.001$.

Acknowledgments: We thank all members of the Guan lab for their support, with particular acknowledgement to Dr. Kaiyuan Liu, Dr. Chenhui Liu, and Tianfu Zhang for their assistance with 2P imaging. We especially appreciate the technical support from the Animal Core Facility and the Molecular Imaging Core Facility at ShanghaiTech University. We want to thank Yazhou Shi (Shanghai Institute of Optics and Fine Mechanics) for his contributions to the initial design and manufacture of the ultraflexible electrode arrays. We also thank Dr. Claus Hilgetag and Dr. Dong Li (UKE Hamburg, Germany) for their suggestions on this work.

Funding:

Science & Technology Innovation 2030 Major Project of China grant (2021ZD0203500) to J.-S.G.

National Natural Science Foundation of China (NSFC) grant (32225023) to J.-S.G.

National Natural Science Foundation of China (NSFC) grant (32400853) to D.Y.

National Natural Science Foundation of China (NSFC) grant (32130043) to H.X.

Central Guidance on Local Science and Technology Development Fund (YDZX20233100001002).

Author contributions:

Conceptualization: J.-S.G., D.Y.;

Investigation: D.Y., Zheng W., S.Z.;

Human ECoG data acquisition: Zhenjie W., J.L., Y.L.;

Manufacture of ultraflexible electrode arrays: H.M., F.H.;

Visualization: D.Y., Zheng W.;

Funding acquisition: J.-S.G., H.X., D.Y.;

Supervision: J.-S.G., H.X.;

Writing – original draft: D.Y.;

Competing interests: The authors declare no competing interests.

Data and materials availability: All data are available in the main text or the supplementary materials.

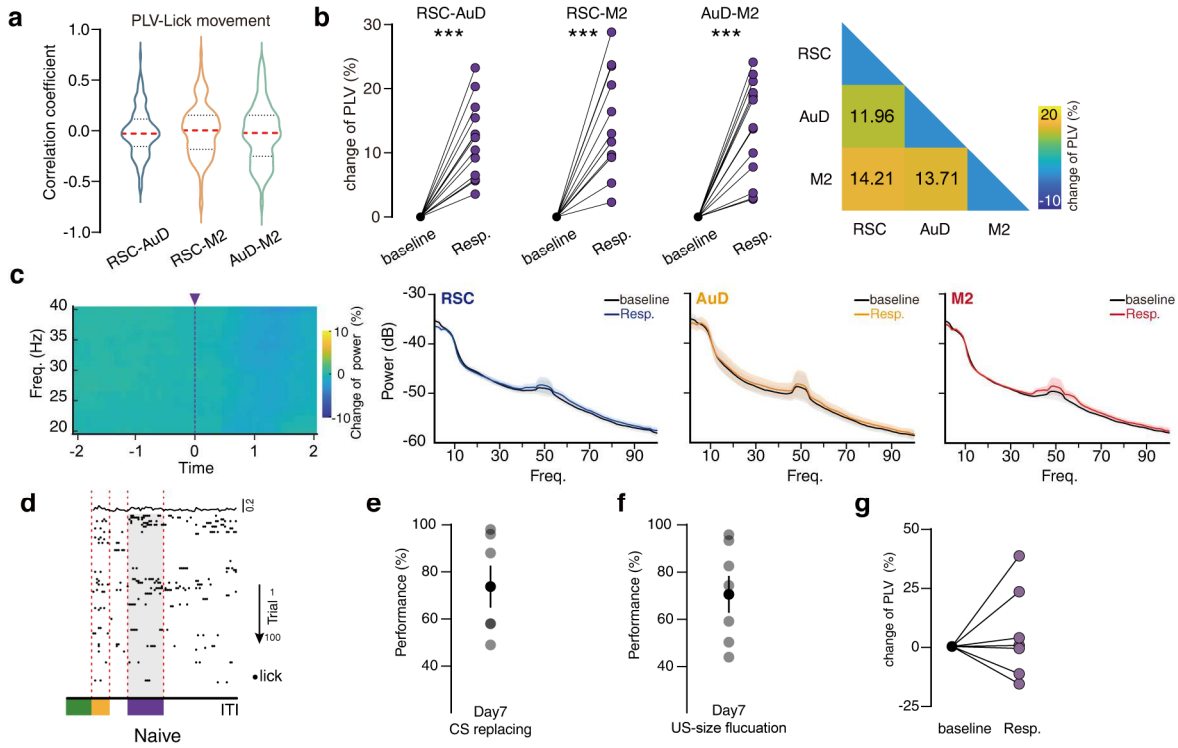

Extended Data Fig. 1

(a) Distribution of correlation coefficients between pairwise γ-synchrony and lick movement. The averaged correlation coefficient for RSC-AuD was -0.014 ± 0.020, for RSC-M2 was 0.018 ± 0.023, and for AuD-M2 was 0.032 ± 0.025.

(b) Contribution of different pairs to the increase in average γ-synchrony during the US period. The average increase in γ-synchrony was 11.96 ± 1.65% for RSC-AuD, 14.21 ± 2.17% for RSC-M2, and 13.71 ± 2.11% for AuD-M2.

(c) The power of γ-oscillations during the US period remained unchanged in the three brain regions compared with the pre-US baseline. The purple triangle and dashed line denote the onset time for US delivery.

(d) The density of licking actions on CS-US training day 1.

(e) The performance of all six mice used in CS replacing experiments on day 7 was 74.50 ± 8.93%.

(f) The performance of all seven mice used in US-size fluctuating experiments on day 7 was 71.41 ± 7.80%.

(g) The relative difference in the average intercortical γ-synchrony between the baseline and response window for trials excluded due to lack of action was 5.37 ± 7.25% (n = 7).

***P <0.001. P values were calculated using two-tailed paired t test (b and g), and multiple t tests (c).

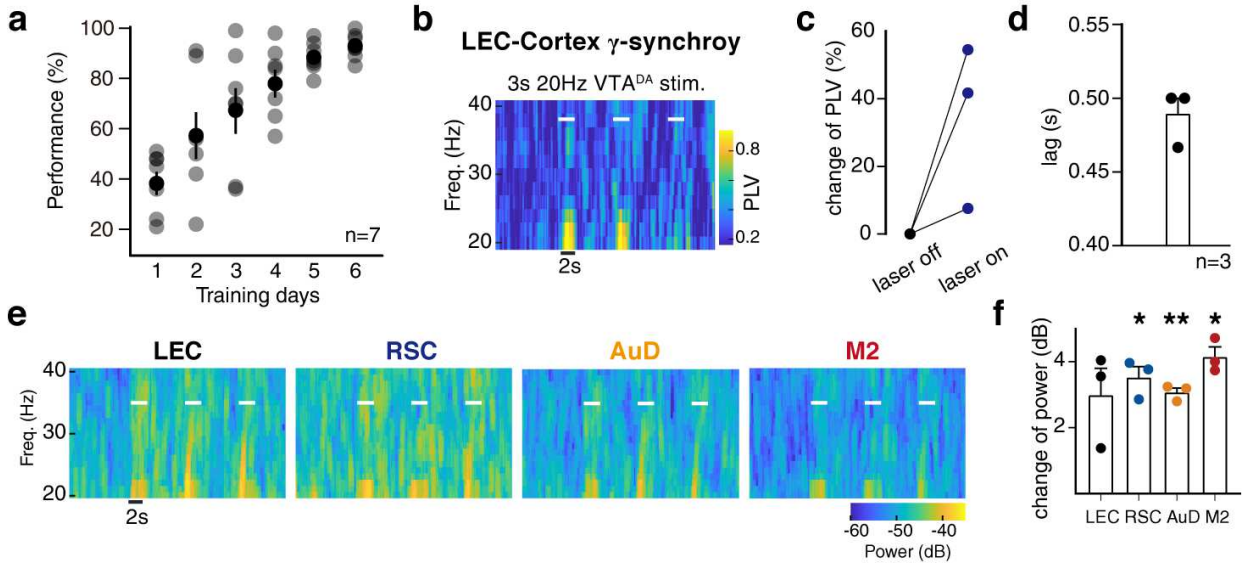

Extended Data Fig. 2

(a) The performance during the CS-US association training for the VTA^{DA} fiber photometry experiment.

(b) Spectrogram of LEC-Cortex γ-synchrony before and after 3-second 20 Hz VTA^{DA} optogenetics stimulation. Top white lines indicate laser stimuli. The spectrogram is an average of all LEC-Cortex pairs, including LEC-RSC, LEC-AuD, and LEC-M2.

(c) The average difference of LEC-Cortex γ-synchrony before and after VTA^{DA} optogenetics stimulation was 34.61 ± 14.61% (P = 0.1322, n = 3). PLV is the average of 3 pairs from 3 mice.

(d) The average response delay time of LEC-Cortices PLV to 20 Hz laser stimulation was 0.49 ± 0.01 s (n = 3).

(e) Spectrogram of low gamma band power change in four brain regions before and after VTA^{DA} optogenetics stimulation.

(f) Low gamma band power change after VTA^{DA} optogenetics stimulation in LEC (3.00 ± 0.82 dB, P = 0.1449), RSC (3.53 ± 0.34 dB), AuD (3.08 ± 0.14 dB), and M2 (4.15 ± 0.29 dB) (n = 3). *P <0.05, **P <0.01. P values were calculated using one-way ANOVA Dunnett's test.

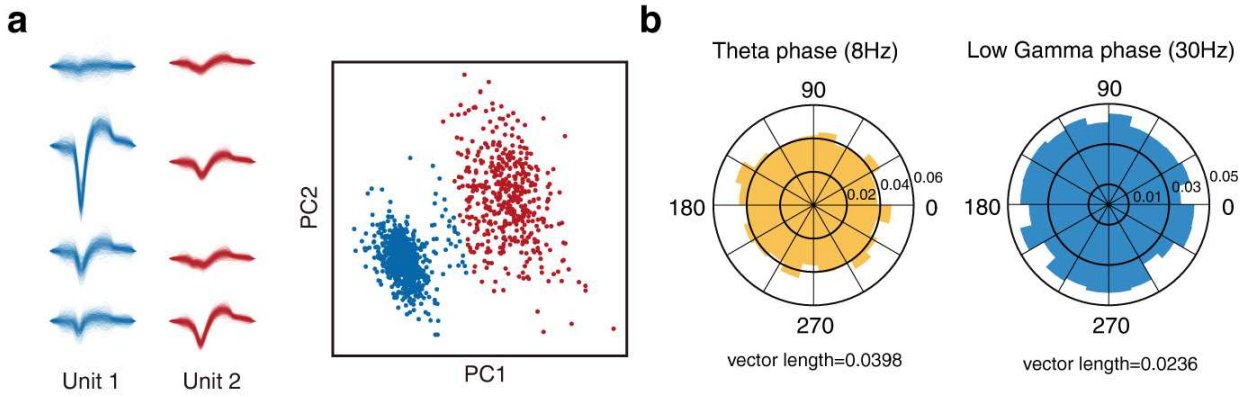

Extended Data Fig. 3

(a) Example of spike sorting results for an optetrode.

(b) Polar plots showing the spike probability of Rbp4-positive cells over Theta phases (yellow, 15° bins) and the low Gamma phase (blue, 15° bins).

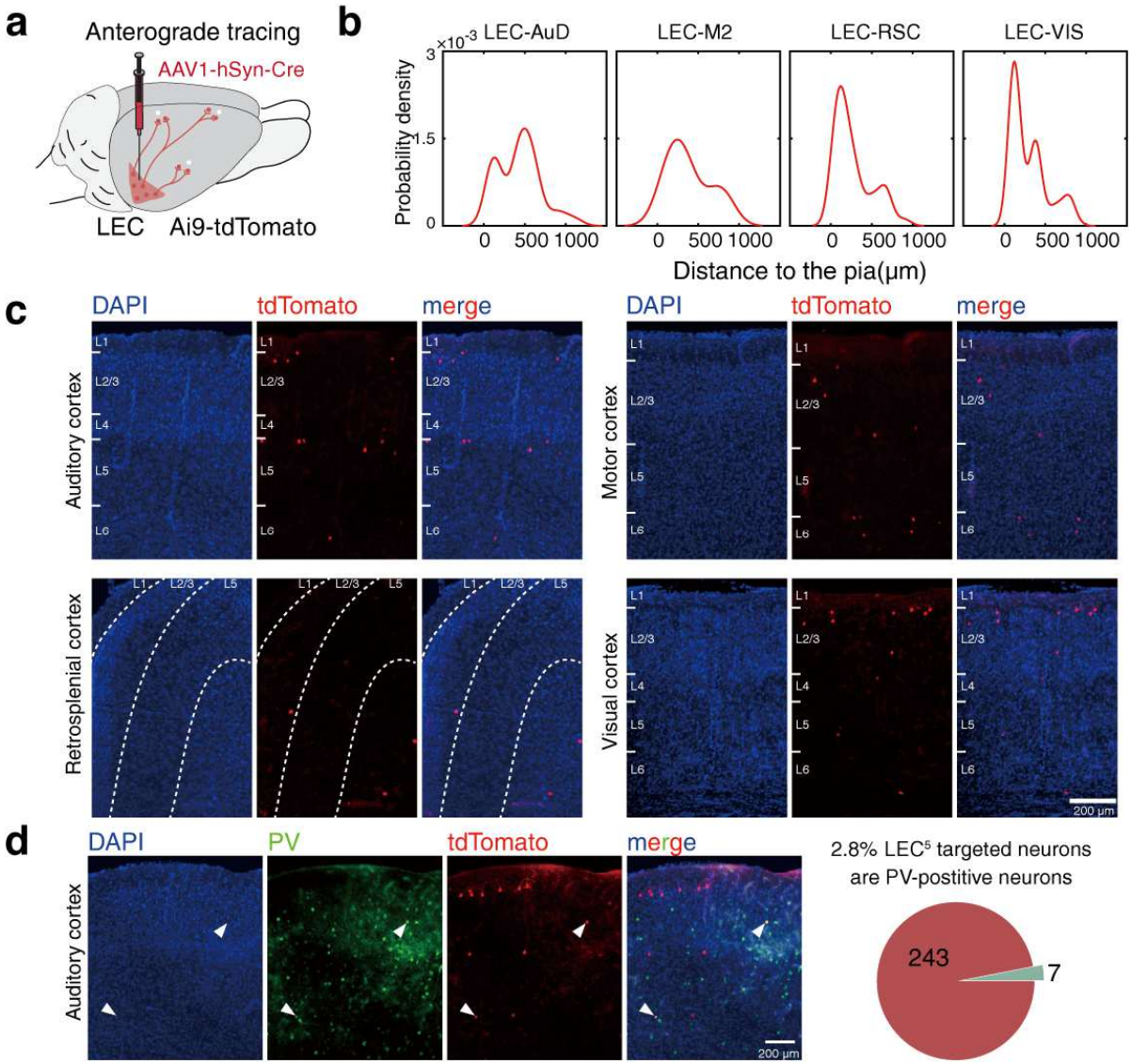

Extended Data Fig. 4

(a) Viral strategy for expressing anterograde trans-synaptic tracing virus AAV1-hSyn-Cre in the LEC area of Ai9 reporter mice.

(b) Quantification of laminar distribution of LEC^5 targeted neurons in AuD, M2, RSC, and VIS (number of neurons: AUD = 199, MO = 11, RSC = 46, VIS = 378, from 3 mice).

(c) Example images of LEC^5 targeted neurons in various cortical areas. Scale bar: 200 μm. The white arrowheads indicate a neuron with double labeling.

(d) Left, representative LEC^5 downstream neurons expressing tdTomato and PV interneurons stained by an antibody (green) in M2. Right, the proportion of PV-positive interneurons among all LEC^5 downstream neurons. A total of 7 PV-positive neurons were identified among the 250 LEC^5 targeted neurons.

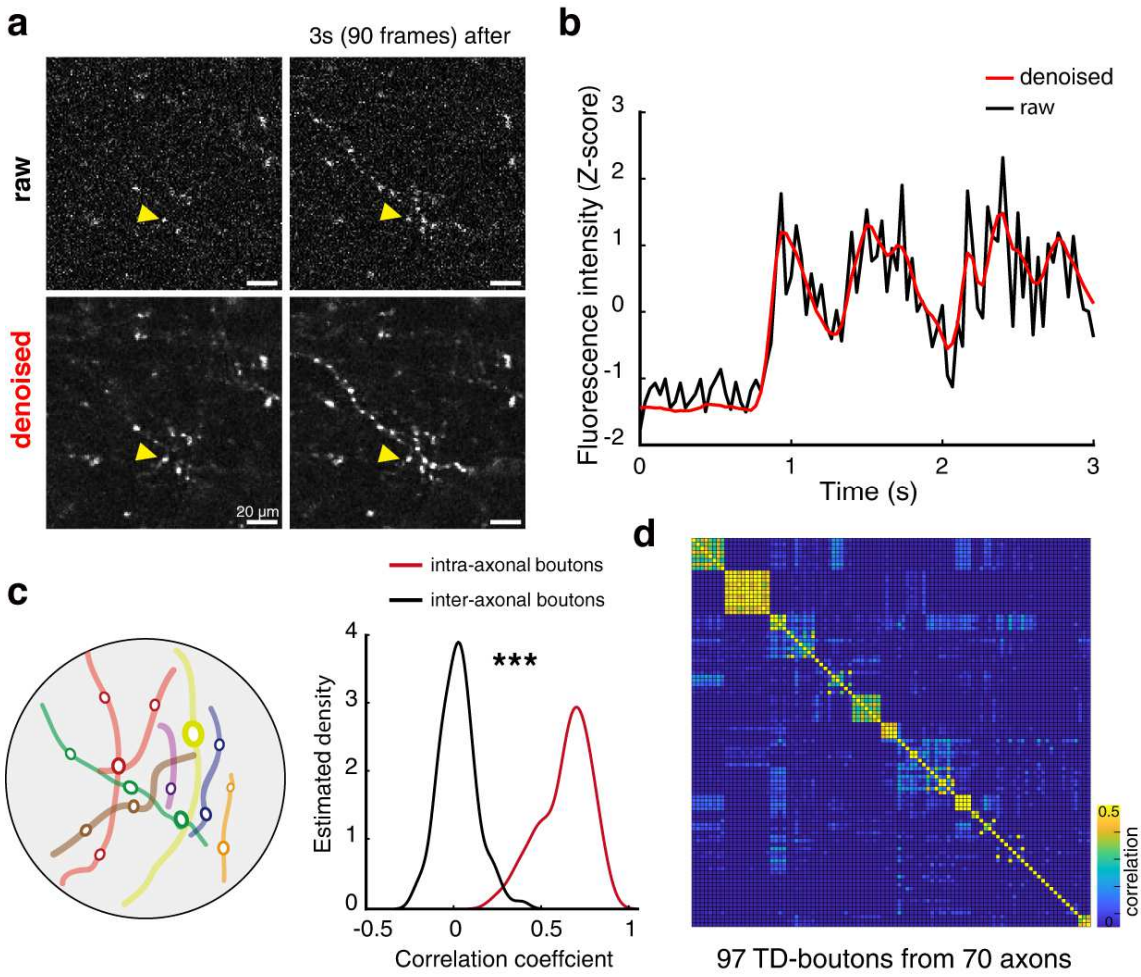

Extended Data Fig. 5

(a) A comparison of the raw image and the image after the implementation of noise reduction with DeepCAD-RT.

(b) A comparison of the normalized intensity of a representative bouton (indicated by a yellow arrowhead in a), before and after noise reduction.

(c) Distribution of correlation coefficients for intra-axonal boutons (red) and inter-axonal bouton pairs (black). ***P <0.001. P values were calculated using Kolmogorov-Smirnov test.

(d) Clustering of 97 TD-boutons based on correlation coefficients identified 70 independent TD-axons from 7 mice.

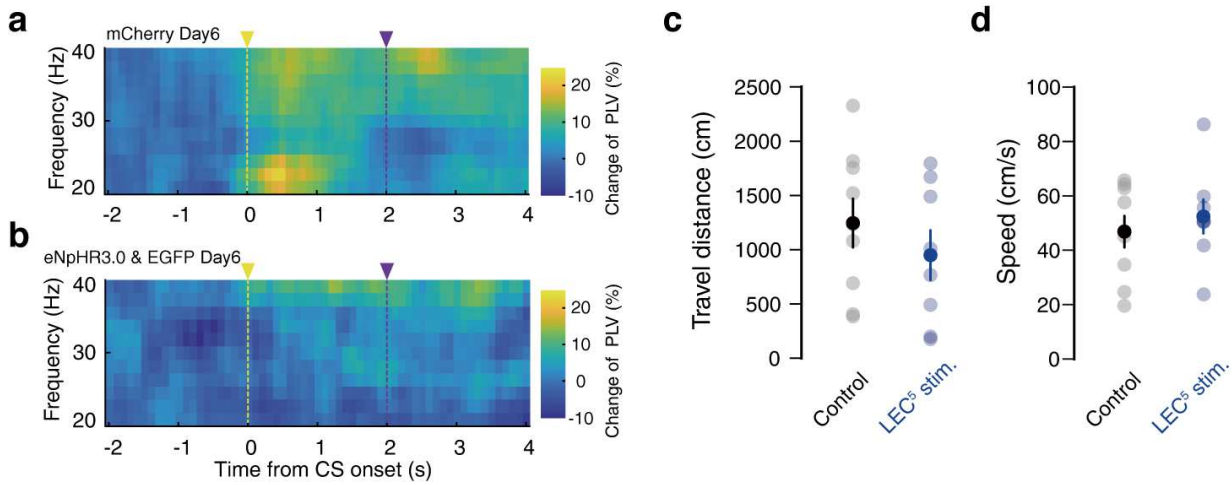

Extended Data Fig. 6

(a) Trial-averaged intercortical γ-synchrony spectrogram of one mouse example in the mCherry control group on day 6.
(b) Trial-averaged intercortical γ-synchrony spectrogram of one mouse example in the EGFP & eNpHR3.0 control group on day 6.
(c) Quantification of the travel distance for the mCherry control group (n = 9) and the oChIEF group (n = 8) of mice during the 3-minute habituation period before the foot shock ($P = 0.37$).
(d) Quantification of the running speed for the mCherry control group (n = 9) and the oChIEF group (n = 8) of mice during the foot shock ($P = 0.52$). *P* values were calculated using t test (c and d).

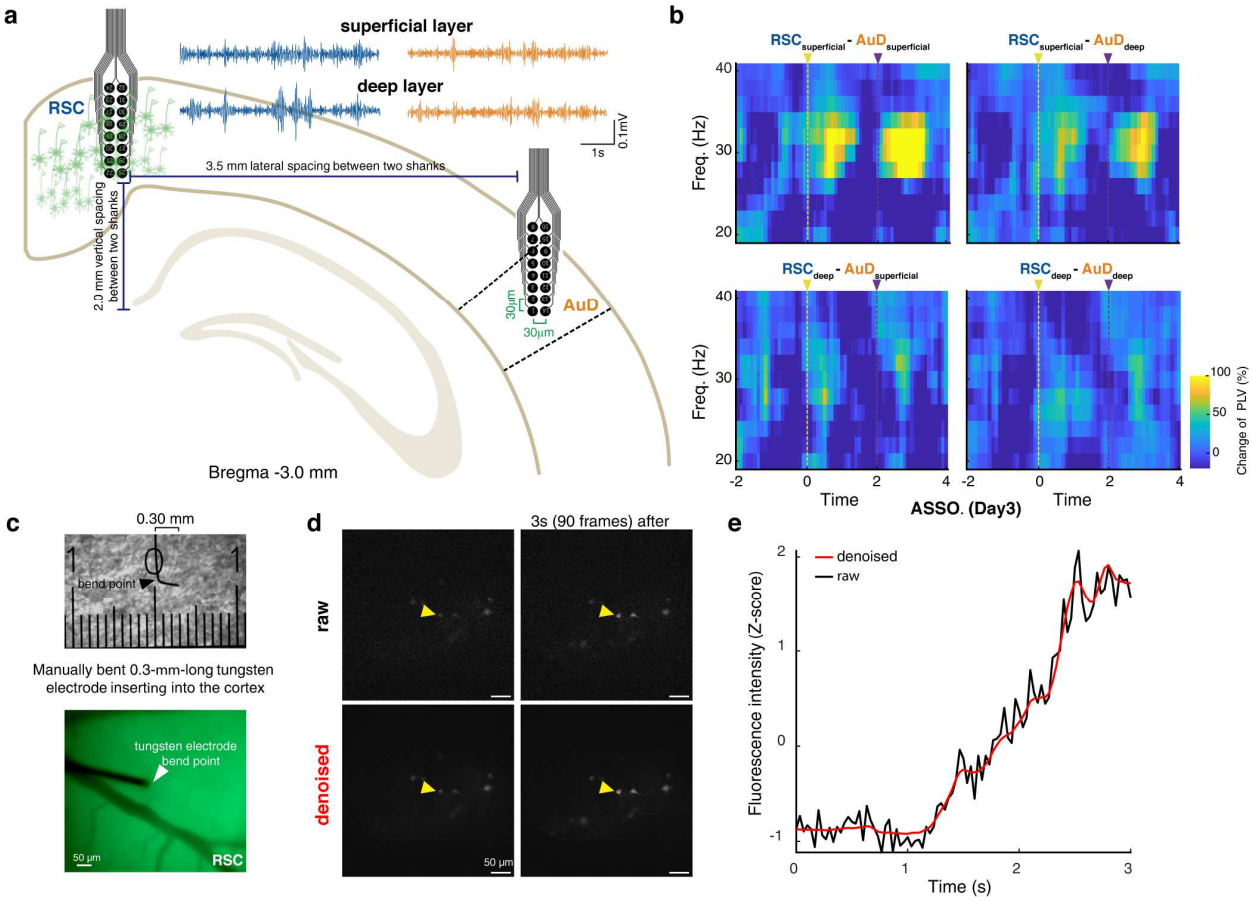

Extended Data Fig. 7

(a) The configuration of 2-shank ultraflexible electrode arrays and typical recording traces (filtered between 20–40 Hz) from superficial and deep recording sites on shanks inserted into the RSC and AuD, respectively. The center-to-center distance between recording sites is 30 mm.
(b) Spectrograms of RSC-AuD γ-synchrony patterns derived from different combinations of LFPs in the deep or superficial regions of the RSC and AuD.
(c) The configuration of the custom-made tungsten electrode used in the 2P imaging experiment.
(d) A comparison of the 2P images before and after the implementation of noise reduction with DeepCAD-RT.
(e) A comparison of the normalized intensity of a representative neuron (indicated by a yellow arrowhead in d), before and after noise reduction.

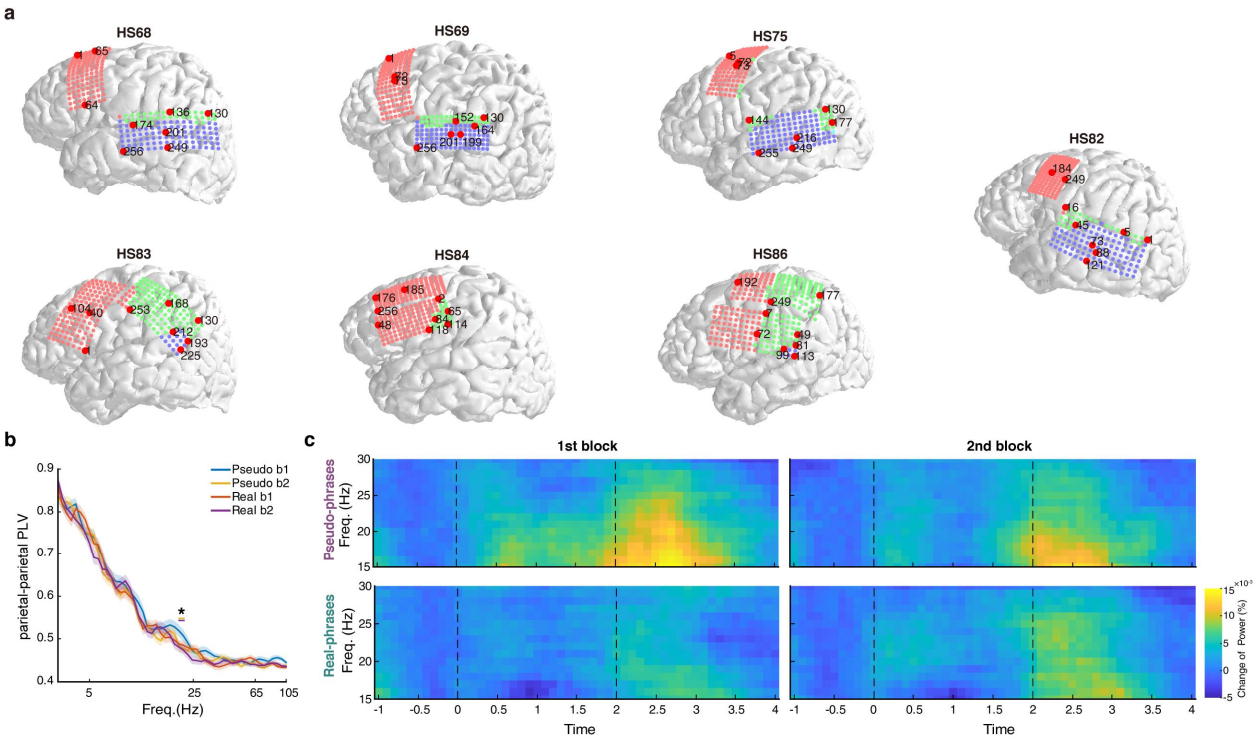

Extended Data Fig. 8

(a) Anatomical placement of the ECoG electrodes in seven patients. The red circles indicate electrode channels located in the frontal lobe, the green circles indicate electrode channels situated in the parietal lobe, and the blue circles indicate electrode channels located in the temporal lobe. The numbers adjacent to the channels denote the channels utilized subsequently for the calculation of the power and pairwise PLV.

(b) A comparison of the average overall synchrony of parietal-parietal pairs within one second after text presentation between pseudo-phrases and real-phrases during the 1st and 2nd blocks. Shading: SEM. 28 pairs from 7 patients. **P* <0.05. *P* values were calculated using multiple t tests.

(c) Low-gamma band power changes in the parietal lobe for pseudo phrases (top) and real phrases (bottom) during the 1st (left) or 2nd (right) blocks, respectively.

Extended Table 1.

Summary of statistical tests for all experiments illustrated in figures.

Figure	Panel	Measure	Group	Statistical test	Test value	*P* value
1	c	8 Hz band intercortical synchrony	Pre-US vs. US	Multiple t tests	t = 2.447	*P* = 0.0144
		20-30 Hz band intercortical synchrony			t = 2.095	*P* = 0.0362
	h	Linear regression of γ-synchrony changes across 6 days	PLV within the response window	Pearson correlation	r^2 = 0.4169	*P* <0.0001
		Linear regression of γ-synchrony changes across 6 days	PLV within the CS period		r^2 = 0.2658	*P* <0.0001
	k	Intercortical γ-synchrony	CS1 vs. CS2	Paired t test	t = 10.65	*P* <0.0001
	n	Linear regression of RPE value and trial-by-trial γ-synchrony within the response window	One mouse example	Pearson correlation	r^2 = 0.5560	*P* <0.0001
		Linear regression of RPE value and trial-by-trial γ-synchrony within the US period			r^2 = 0.0114	*P* = 0.2786

	o	Linear regression of RPE value and trial-by-trial γ-synchrony within the response window	All seven mice	Pearson correlation	$r^2 = 0.3903$	$P < 0.0001$
		Linear regression of RPE value and trial-by-trial γ-synchrony within the US period			$r^2 = 0.001$	$P = 0.4035$
2	d	Linear regression of day-by-day γ-synchrony change within the CS period and averaged VTA^{DA} activity	All six mice	Pearson correlation	$r^2 = 0.7972$	$P = 0.0166$
	e	Time lag between VTA^{DA} activity and the increase in γ-synchrony	time lags vs. zero	t test	t = 4.393	$P < 0.0001$
	h	Intercortical γ-synchrony	before vs. after stimulation	Paired t test	t = 9.044	$P = 0.0120$
	i	Time lag between the stimulation and the increase in γ-synchrony	time lags vs. zero	Paired t test	t = 8.162	$P = 0.0147$
	l	Normalized firing rate change	baseline vs. CS sti.	one-way ANOVA Tukey test	F = 51.55	$P = 0.9830$

			baseline vs. US sti.			P <0.0001
		Normalized firing rate change	baseline vs. CS period	one-way ANOVA Tukey test	F = 10.64	P = 0.0049
			baseline vs. response window			P = 0.0213
			CS period vs. response window			P = 0.2870
	q	Averaged calcium activity	first five US-only trials vs. last five US-only trials	Kolmogorov-Smirnov test	KS distance = 0.0980	P <0.0001
	v	Averaged calcium activity within the CS period	1st Asso. vs. D-US	one-way ANOVA Tukey test	F = 1.121	P = 0.6175
			1st Asso. vs. US-omi.			P = 0.9633
			1st Asso. vs. 2nd Asso.			P = 0.6879
			D-US vs. US-omi.			P = 0.6884
			D-US vs. 2nd Asso.			P = 0.4235
			US-omi. vs. 2nd Asso.			P = 0.9500
		Averaged calcium activity	1st Asso. vs. D-US	one-way ANOVA Tukey test	F = 95.06	P <0.0001

		within the US period	1st Asso. vs. US-omi.			*P* <0.0001
			1st Asso. vs. 2nd Asso.			*P* = 0.9676
			D-US vs. US-omi.			*P* <0.0001
			D-US vs. 2nd Asso.			*P* <0.0001
			US-omi. vs. 2nd Asso.			*P* <0.0001
3	e	Intercortical γ-synchrony	mCherry group baseline vs. US	Paired t test	t = 7.060	*P* = 0.0004
			eNpHR3.0 group baseline vs. US		t = 0.5550	*P* = 0.5962
	f	Day-by-day performance	day1 mCherry vs. eNpHR3.0	Multiple t tests Holm-Sidak method	t = 0.7781	*P* = 0.4504
			day2 mCherry vs. eNpHR3.0		t = 1.547	*P* = 0.3401
			day3 mCherry vs. eNpHR3.0		t = 1.619	*P* = 0.3401
			day4 mCherry vs. eNpHR3.0		t = 3.746	*P* = 0.0122
			day5 mCherry vs. eNpHR3.0		t = 6.498	*P* <0.0001

			day6 mCherry vs. eNpHR3.0		t = 3.402	*P* = 0.0208
	k	Intercortical γ-synchrony	EGFP&eNpHR3.0 group baseline vs. US	Paired t test	t = 1.191	*P* = 0.2870
			oChIEF&eNpHR3.0 group baseline vs. US		t = 5.964	*P* = 0.0010
	l	Day-by-day performance	day1 oChIEF&eNpHR3.0 vs. EGFP&eNpHR3.0	Multiple t tests Holm-Sidak method	t = 8.624	*P* <0.0001
			day2 oChIEF&eNpHR3.0 vs. EGFP&eNpHR3.0		t = 8.470	*P* <0.0001
			day3 oChIEF&eNpHR3.0 vs. EGFP&eNpHR3.0		t = 6.040	*P* <0.0001
			day4 oChIEF&eNpHR3.0 vs. EGFP&eNpHR3.0		t = 5.383	*P* <0.0001
			day5 oChIEF&eNpHR3.0 vs. EGFP&eNpHR3.0		t = 4.988	*P* <0.0001
			day6 oChIEF&eNpHR3.0 vs.		t = 3.060	*P* = 0.0109

			EGFP&eNpHR3.0			
		Block-by-block performance on day 1	Block1 oChIEF&eNpHR3.0 vs. EGFP&eNpHR3.0	Multiple t tests Holm-Sidak method	t = 2.039	*P* = 0.0687
			Block2 oChIEF&eNpHR3.0 vs. EGFP&eNpHR3.0		t = 5.377	*P* = 0.0009
			Block3 oChIEF&eNpHR3.0 vs. EGFP&eNpHR3.0		t = 4.178	*P* = 0.0039
			Block4 oChIEF&eNpHR3.0 vs. EGFP&eNpHR3.0		t = 6.359	*P* <0.0001
			Block5 oChIEF&eNpHR3.0 vs. EGFP&eNpHR3.0		t = 13.92	*P* <0.0001
	n	Preference index	Contrl day1 vs. day3	two-way ANOVA Tukey test	F = 10.02	*P* = 0.0365
			LEC[5] stim. day1 vs. day3		F = 10.02	*P* = 0.0425
			LEC[5] stim. day5 vs. control day5		F = 2.364	*P* = 0.0258
			LEC[5] stim. day5 vs. day1		F = 10.02	*P* = 0.0254

	q	Freezing level	immediate recall LEC^5 stim. vs. control	t test	t = 0.4350	$P = 0.6697$
			24h recall LEC^5 stim. vs. control	t test	t = 2.506	$P = 0.0242$
4	g	Linear regression of γ-synchrony change and activity of latent RSC Engram	One RSC Engram example	Pearson correlation	$r^2 = 0.2227$	$P = 0.0112$
	h	Pearson correlation coefficient	Engram vs. non-Engram	Kolmogorov-Smirnov test	KS distance = 0.3907	$P = 0.0102$
	i	Time lag between the rising time of latent RSC Engrams and the increase in γ-synchrony	day3 vs. day7	Paired t test	t = 2.477	$P = 0.0234$
5	d	Average overall synchrony of parietal-parietal pairs within a 1s time segment after a phrase presentation	pseudo-phrases block1 vs. pseudo-phrases block2	one-way ANOVA Tukey test	F = 5.791	$P = 0.0310$
			pseudo-phrases block1 vs. real-phrases block1			$P = 0.0151$
			pseudo-phrases block1 vs. real-phrases block2			$P = 0.0082$

			pseudo-phrases block2 vs. real-phrases block1			*P* = 0.9999
			pseudo-phrases block2 vs. real-phrases block2			*P* = 0.9628
			real-phrases block1 vs. real-phrases block2			*P* = 0.9627
Extended Data Fig. 1	b	Low Gamma band RSC-AuD PLV	Pre-US vs US	Paired t test	t = 7,237	*P* <0.0001
		Low Gamma band RSC-M2 PLV			t = 6.552	*P* <0.0001
		Low Gamma band AuD-M2 PLV			t = 6.501	*P* <0.0001
	c	Averaged oscillation power	RSC Pre-US vs US	Multiple t tests		*P >0.05*
			AuD Pre-US vs US			*P >0.05*
			M2 Pre-US vs US			*P >0.05*
	g	Intercortical γ-synchrony in the excluded trials	baseline vs. response window	Paired t test	t = 0.7404	*P* = 0.4870
Extended Data Fig. 2	c	Intercortical γ-synchrony	LEC-Cortex γ-synchrony before vs. after stimulation	Paired t test	t = 2.470	*P* = 0.1322

	d	Time lag between the stimulation and the increase in LEC-Cortex γ-synchrony	time lags vs. zero	Paired t test	t = 44.00	*P* <0.0001
	f	Averaged oscillation power	LEC before vs. after stimulation	one-way ANOVA Dunnett's test	F = 15.09	*P* = 0.1449
			RSC before vs. after stimulation			*P* = 0.0203
			AuD before vs. after stimulation			*P* = 0.0045
			M2 before vs. after stimulation			*P* = 0.0110
Extended Data Fig. 5	c	Averaged calcium activity	inter-axons vs. intra-axons	Kolmogorov-Smirnov test	KS distance = 0.9667	*P* <0.0001
Extended Data Fig. 6	c	Travel distance during the 3-minute habituation period	mCherry vs. OChIEF	t test	t = 0.9231	*P* = 0.3706
	d	Running speed during foot shock			t = 0.6534	*P* = 0.5234
Extended Data Fig. 8	b	Parietal-parietal synchrony	pseudo block1 vs. pseudo block1	Multiple t tests	t = 2.113	*P* = 0.0346
			pseudo block1 vs. real block1		t = 1.845	*P* = 0.0650
			pseudo block1 vs. real block2		t = 2.269	*P* = 0.0233

Extended Table 2.

Primary antibodies and secondary antibodies used for immunofluorescence experiments.

Primary antibody information			
Target	**Host**	**Vendor**	**Product Number**
Tyrosine Hydroxylase	Rabbit	Cell Signaling Technology, USA	13106
Parvalbumin	Rabbit	Cell Signaling Technology, USA	80561
mCherry	Mouse	Abclonal, China	AE002
GFP	Rabbit	Abclonal, China	AE078
Secondary antibody information			
Antibody	**Alexa Fluorophore**	**Vendor**	**Product Number**
Goat-anti-Rabbit	488	Yeasen, China	33106ES60
Goat-anti-Mouse	555	Thermo Fisher Scientific, USA	A-21422

Extended Table 3.

Placement of the ECoG electrode for each patient.

Region / Patient	Frontal lobe	Parietal lobe	Temporal lobe	Occipital lobe
HS68	129	36	91	0
HS69	129	36	91	0
HS75	124	29	102	1
HS82	130	27	99	0
HS83	138	102	16	0
HS84	232	24	0	0
HS86	125	124	7	0

Extended Table 4.

Summary of the number of pairs in each patient used for PLV calculation.

Pairs / Patient	Frontal-Frontal	Frontal-Parietal	Frontal-Temporal	Parietal-Parietal	Parietal-Temporal	Temporal-Temporal
HS68	3	9	9	3	9	3
HS69	3	9	9	3	9	3
HS75	3	9	9	3	9	3
HS82	3	9	9	3	9	3
HS83	3	9	9	3	9	3
HS84	10	20	0	6	0	0
HS86	3	9	9	3	9	3